




Cite this: *Mater. Adv.*, 2025,  
6, 5648

## Design and DFT-based optimization of a GO-containing guar gum hydrogel for dye removal†

Reyaz Ahmad Rather, Jan Mohammad Mir,  Mushtaq Ahmad Bhat and Aabid Hussain Shalla\*

A superabsorbent hydrogel composed of graphene oxide (GO), guar Gum (GG), and resorcinol (Res), cross-linked by lanthanum nitrate trihydrate ( $\text{La}^{3+}$ ) ions, was synthesized through the solvent rotation method. All the components involved in the formation of the hydrogel complex were optimized separately using the Gaussian16W/GaussView6.1 software package and density functional theory (DFT), followed by the optimization of the complex and the target dye crystal violet (CV). The Stuttgart–Dresden (SDD) basis set and the WB97XD functional were used for the GO–GG–Res– $\text{La}(\text{III})$  complex, and for the rest of the computations, the combination of B3LYP functional and 6-311G(d,p) basis set was used. To correlate the adsorption of CV with the designed hydrogel, the key electronic structures and the covalent and non-covalent factors responsible for the adsorbent behaviour were examined. Moreover, molecular orbital energies, electronegativity, ionization energy, electron affinity, and other global reactive descriptors were explained in the context of the aim of this study. Experimentally, the prepared hydrogel exhibited significant swelling behaviours in water across solutions of varying ionic strengths and pH environments for both GO and non-GO beads. The equilibrium elimination capacity of the crystal violet (CV) dye increased from 134.88  $\text{mg g}^{-1}$  to 234.32  $\text{mg g}^{-1}$  in deionized water and from 226.66  $\text{mg g}^{-1}$  to 241.09  $\text{mg g}^{-1}$  at pH 9, both with and without graphene oxide (GO), respectively. Various kinetic adsorption isotherms were also applied. The enhanced dye removal efficacy of CV supported by the DFT integrated experimental studies, indicates the potential of these hydrogel beads in wastewater treatment.

Received 23rd April 2025,  
Accepted 22nd June 2025

DOI: 10.1039/d5ma00389j

rsc.li/materials-advances

## 1. Introduction

Fast industrialization and population growth are the two primary aspects of the modern world that are primarily responsible for the increased release of hazardous pollutants, including pharmaceuticals, biomedical, dyes, heavy metals, and pesticides, into the environment. The accelerated production and use of such hazardous materials have caused devastating environmental issues, which are primarily related to air, soil, and water. Water pollution is a major pollution caused by industries that frequently release dyes, heavy metals, and various other organic pollutants.<sup>1,2</sup> Dyes such as methylene blue (MB), methyl red (MR), and crystal violet (CV) are known for their carcinogenic nature.<sup>3</sup> The CV dye falls in the category of triarylmethane-based systems, and in aqueous solution, it

transmits a violet color. All these organic dyes, including CV, have severe impacts on human health and marine life, even at low concentrations.<sup>4</sup> These dyes could induce hazardous effects on the eyes and skin, and inhaling them causes digestive tract irritation.<sup>5</sup> Among the vast number of such pollutants, synthetically prepared dyes produce toxic chemicals with carcinogenic nature *via* different processes, causing severe harm to the environment and to the overall health of humans and animals.<sup>6,7</sup> In the aquatic environment, these dye molecules inhibit photosynthetic activity due to a reduction in light transmittance.<sup>8,9</sup> In the water treatment, desalination and purification industries, hydrogels are the first choice of material. In most cases, they are made up of either synthetic or natural polymers and are suitable for the removal of a broad variety of pollutants, including dyes, agricultural wastes, pesticides, and heavy metal ions, which are particularly found in water.<sup>29</sup> For the removal of water pollutants, mainly dyes, numerous methods have been used for water treatment, including chemical deposition, ion exchange,<sup>10</sup> adsorption,<sup>11–13</sup> coagulation–flocculation,<sup>11</sup> photocatalytic degradation,<sup>14</sup>

Soft Chemistry Lab, School of Sciences, Islamic University of Science and Technology, IUST Awantipora, J&K, 192122, India. E-mail: Sheenf@gmail.com

† Electronic supplementary information (ESI) available. See DOI: <https://doi.org/10.1039/d5ma00389j>



membrane separation,<sup>15</sup> and adsorption and photocatalytic remediation.<sup>16,17</sup> Among these methods, adsorption is one of the most acceptable and widely used techniques owing to its inexpensive, easy-to-design, and more effective nature than other methods.<sup>18</sup> Hydrogels have been widely studied as low-cost, green adsorbent materials with excellent adsorption capacity for dyes.<sup>19</sup> Numerous studies on the removal of different contaminants from wastewater and aqueous media have focused on GG hydrogels.<sup>20</sup> Furthermore, a few GG-based interpenetrating networks have been developed, characterized, and used as intelligent superabsorbent hydrogels for commercial purposes.<sup>21</sup> The mechanical properties and workability of GG were discovered to improve when reinforced with various inorganic compounds. GG-based nanocomposites with various inorganic cores, including clay and SiO<sub>2</sub>, have recently been studied for wastewater remediation.<sup>22</sup> The inorganic material is spread across the guar gum-inorganic composites crosslinked networks. The microwave-assisted synthesis of GG-carboxymethyl cellulose hydrogel was covalently crosslinked using epichlorohydrin as a crosslinker. CV and brilliant green dye were successfully removed using the prepared hydrogel, and the removal percentage was found to be up to about 96.78 and 94.01% for CV and brilliant green dyes, respectively.<sup>23</sup> The microwave-assisted grafting method was employed for the synthesis of GG-acrylic acid hydrogel reinforced with nano clay and multiwalled carbon nanotubes, and was used for the removal of CV dye from aqueous solutions. Among the prepared hydrogels, the one with multiwalled carbon nanotubes shows maximum adsorption than the other ones.<sup>24</sup> Furthermore, guar gum-based polysaccharides have several advantages over other hydrogel-forming polymers, like biodegradability, ease of availability, low cost, and simple methods of modification for numerous applications. Furthermore, GO, which presents a 2D surface architecture with nanodimensions with oxygen-containing functionalities, renders it compatible with water-soluble polymers.<sup>25,26</sup> The presence of GO in the hydrogel network leads to more stable and effective hydrogel having potentially favourable in water-related applications. The functionalities of GO containing epoxy, hydroxyl, carboxyl and carbonyl groups in general improve the mechanical strength and thermal stability and also enhances the adsorption capabilities hydrogels.<sup>27,28</sup> Furthermore, the surface charge due to these functional groups makes GO a good adsorbent for the removal of dyes, particularly cationic dyes, from aqueous solutions.

Lanthanum nitrate (La<sup>3+</sup>) is an effective crosslinker for hydrogel beads due to its strong ionic interactions with negatively charged polymers like alginate, CMC, or GG. Its trivalent nature offers stronger bonding than divalent ions (e.g., Ca<sup>2+</sup>, Mg<sup>2+</sup>), enhancing gelation control and enabling precise bead formation. These interactions also improve the hydrogel's mechanical and thermal stability.<sup>29</sup> Compared to classic crosslinkers such as Ca<sup>2+</sup>, Fe<sup>3+</sup>, or synthetic agents like *N,N'*-methylenebisacrylamide (MBA), La<sup>3+</sup> has different advantages. Higher charge density improves the crosslinking and mechanical strength of the hydrogel. La<sup>3+</sup>-crosslinked

hydrogels adsorb cationic dyes like crystal violet due to their expanded binding sites and stronger electrostatic interactions. These hydrogels also retain structural integrity after numerous adsorption-desorption cycles, thereby improving long-term stability. Research indicates that adding La<sup>3+</sup> as a crosslinker to hydrogel systems improves CV dye adsorption and removal from aqueous solutions. The trivalent character of La<sup>3+</sup> facilitates strong electrostatic interactions between the negatively charged functional groups in the hydrogel and cationic dye molecules. The higher crosslinking density creates more dye-adsorption sites, thereby increasing the removal capacity.<sup>30</sup>

In association with the experimental techniques used to discuss adsorption chemistry, density functional theory (DFT) is an advanced tool for evaluating and validating the same. The application of DFT in predicting and establishing conformational analysis is conspicuous from the scientific reports published in the last two decades.<sup>31</sup> DFT can be used to study hydrogel interaction geometry, frontier orbital analysis, electron density mapping, charge distribution exploration, charge transfer analysis, and hyperpolarizability. These aspects, in turn, help in understanding the covalent and non-covalent interaction (NCI) meant for explaining various mechanistic approaches. Its application in understanding hydrogel adsorption is becoming increasingly crucial for designing more efficient and selective hydrogel-based adsorbents.<sup>32,33</sup> The selection of basis sets and functionals has a significant effect on such studies. The speculation of dye adsorption represents a highly fascinating area, and hence, it becomes easy to identify and validate a selected adsorbent using DFT.

CV dye was chosen as this is included in the category of cationic dyes and is widely used in various industries, such as pharmaceuticals, paper, textiles, and printing inks. In addition to having medical uses, this dye can be very dangerous if inhaled or consumed and can cause eye irritation, increased heart rate, permanent blindness, skin irritation and cyanosis in the human body.<sup>34</sup> Furthermore, it is toxic to aquatic organisms, potentially mutagenic and carcinogenic, and bioaccumulates in the food chain. Due to its chemical stability and biodegradation resistance, CV persists in aquatic environments, making it difficult to remove using conventional treatment methods. Even at low concentrations, it causes aesthetic pollution and disrupts photosynthesis by limiting light penetration in water.<sup>35,36</sup> Considering the harmful effects of CV dye, this study examines the adsorption performance of a newly developed hydrogel composed of GG, Res and GO, which were crosslinked using La<sup>3+</sup>(aq) metal ions to form hydrogel beads. The removal of cationic CV dye from aqueous solutions was assessed, and the adsorption mechanism of the hydrogel was evaluated through kinetic and isotherm studies.

## 2. Experimental

All key experimental measurements were performed in triplicate, and the average value is presented in the manuscript. Regarding instrumentation, the background correction and



baseline calibration were performed before each measurement for UV-vis, TGA, and FTIR analyses, following standard protocols. The synthesis, swelling and dye removal applications of hydrogel beads were performed at room temperature (25 °C) and neutral pH (pH ~ 7).

## 2.1. Materials

Guar gum (GG), resorcinol (Res), lanthanum nitrate hexahydrate ( $\text{La}^{3+}(\text{aq})$ ), Sodium hydroxide (NaOH), PBS buffer and hydrochloric acid (HCl). All chemicals were obtained directly from Sigma-Aldrich India.

## 2.2. Methods

**2.2.1. Synthesis of the GO.** An improved or slightly modified Hummers' method using graphite powder was used for the successful preparation of GO. This method primarily involves pouring a mixture of graphite powder (3.0 g) and  $\text{KMnO}_4$  (18.0 g) into a 9:1 ratio of concentrated  $\text{H}_2\text{SO}_4$  and  $\text{H}_3\text{PO}_4$  (360:40 mL). The exothermic reaction raised the temperature of the mixture up to ~40 °C. The temperature was raised to 50 °C and kept on a magnetic stirrer (300 rpm) following vigorous stirring for almost 12 h. The resultant mixture turns into a dark green suspension. Furthermore, the suspension is cooled to room temperature, followed by the addition of ice cubes of 400 mL and then 3.0 mL of  $\text{H}_2\text{O}_2$  solution (30 wt%) is mixed dropwise. A brown precipitate is obtained. This suspension was filtered, centrifuged (5000 RPM for every 5 min) and frequently washed with MQ water, aqueous HCl solution (30%) and finally with ethanol (200 mL each) three times. Finally, the mixture was coagulated by adding 250 mL of ether, and the resultant suspension was filtered using polytetrafluoroethylene (PTFE) filter paper containing 0.45  $\mu\text{m}$  pore size. The final product was filtered and dried in a vacuum overnight at room temperature, yielding 5.8 g of product.<sup>37–40</sup>

**2.2.2. Synthesis of GG-Res-La and GG-Res-La-GO hydrogel beads.** A fixed amount of GG (250 mg) and Res (100 mg) was dissolved in 10 mL of distilled water and stirred using a magnetic stirrer. A 0.5 M solution of  $\text{La}^{3+}(\text{aq})$  was also prepared in distilled water. A stock solution of GO was prepared by sonicating the already prepared GO sheets in distilled water for about 30 minutes. 0.5 M solution of sodium hydroxide was also prepared. To form a homogenous solution, 3 mL of Res solution was added to the polymer solution (GG), after which 0.5 mL of  $\text{La}^{3+}$  was added. Furthermore, a predetermined quantity of 1 mL GO (0.5, 1.0, and 1.5  $\text{mg mL}^{-1}$ ) aqueous dispersion was added and stirred for 2 h using a magnetic stirrer. The resulting homogenous mixture was poured into the 50 mL NaOH solution with a 22-gauge needle on a magnetic stirrer at 400 rpm to form the spherical hydrogel beads. The beads were kept in NaOH solution for approximately 2 h. The hydrogel beads were then filtered and washed several times with deionised water and allowed to freeze dry (–79 °C) for a minimum of 72 h. The additional hydrogel bead samples were obtained by the addition of variable GO (0.5, 1.0 and 1.5  $\text{mg mL}^{-1}$ ) and designated as GG-Res-La-GO1, GG-Res-La-GO2, and GG-Res-La-GO3. In addition, as a control sample

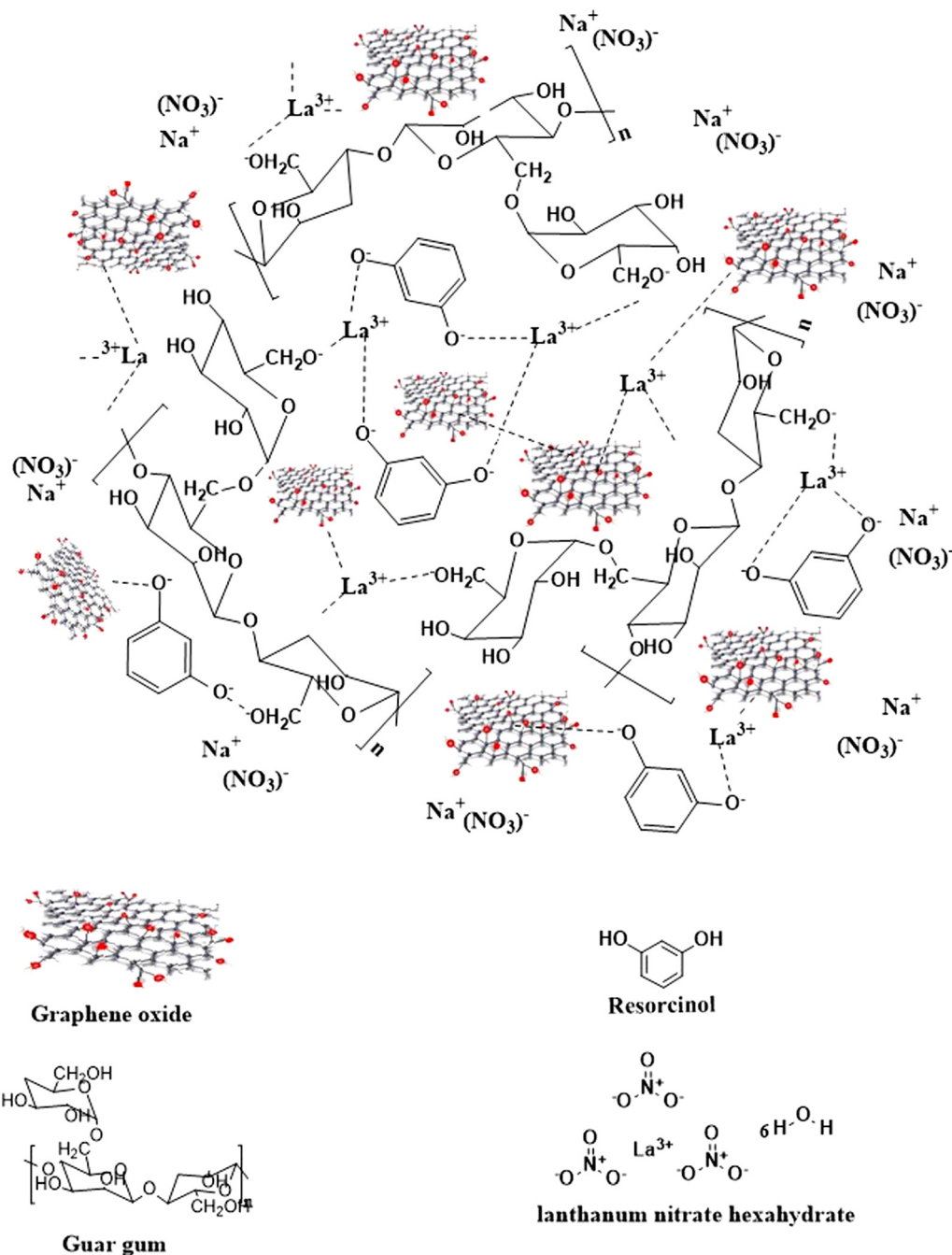
(GG-Res-La), hydrogel beads without GO were prepared using the same procedural steps. The whole procedure was performed at room temperature (25 °C) at neutral pH (pH ~ 7). We conducted triplicate syntheses and measured the bead diameter. The results showed a minimal standard deviation in bead size, indicating good reproducibility. Regarding residual  $\text{La}^{3+}$  content, it was found to be below detectable limits, confirming minimal retention and supporting the material's environmental safety for practical applications. The possible reaction mechanism for the formation of a hydrogel bead is shown in Scheme 1. The formation of  $\text{La}^{3+}$ -crosslinked hydrogel beads involves coordination, hydrogen bonding among GG, GO, and Res.  $\text{La}^{3+}$  ions coordinate with carboxylate and hydroxyl groups on GG and GO, forming strong ionic bridges that enhance the network's mechanical strength. Additionally, abundant –OH groups on GG, GO, and Res enable extensive hydrogen bonding, further stabilizing the hydrogel matrix through physical entanglement of the polymer chains. In NaOH, GG and Res are deprotonated, converting OH to alkoxide ions ( $\text{O}^-$ ), increasing the nucleophilicity of GG and Res, making them more reactive toward electrophilic agents (e.g., epoxides, aldehydes, or  $\text{La}^{3+}$  coordination sites). The deprotonated –OH groups can also engage in hydrogen bonding or intermolecular reactions with other functional groups (such as –COOH or –OH) on polymers.<sup>41,42</sup>

**2.2.3. DFT-based optimization, FMO analysis, charge distribution, and hyperpolarizability.** The energy minimal state or optimized structural conformation of the target complex was obtained by optimizing at the DFT level Stuttgart–Dresden (SDD) basis set along with WB97XD as a functional. GAUSSIAN 16W and GaussView6.1 were the software packages used for the calculations, and for the rest of the computations done for the components of the complex and CV, the B3LYP functional and 6-311G(d,p) basis set combination were used. Various systematic algorithms under combined non-planar group symmetry and theoretical force constants generate useful conclusions from the calculation. Molecular orbital analysis and the inclusion of Koopman's theorem-based<sup>43</sup> results were further analysed using various derivative formulas. The high value of the highest occupied molecular orbital (HOMO) and the low value of the lowest unoccupied molecular orbital (LUMO) in a complex can indicate a strong tendency for adsorption, as these values suggest a high reactivity and potential for interaction with other molecules. In the context of crystal violet (CV) adsorption on hydrogels, this principle can be applied to understand the adsorption mechanisms and efficiency. The papers provided offer insights into the adsorption properties of various hydrogels, which can be related to the HOMO–LUMO values and their implications for CV adsorption. Electronegativity in terms of FMO energies, ionization energy (IE), electron affinity (EA), and the related parameters, absolute electronegativity ( $\chi_{\text{abs}}$ ), absolute hardness ( $\eta$ ), electrophilicity index ( $\omega$ ), and global softness ( $S$ ) were computed as follows:

$$E_{\text{HOMO}} = \text{IE} \quad (1)$$

$$-E_{\text{LUMO}} = \text{EA} \quad (2)$$





**Scheme 1** Possible mechanistic interactions in the prepared hydrogel beads under alkaline conditions.

$$\chi_{\text{abs}} = \frac{(\text{IE} + \text{IA})}{2} = \frac{(E_{\text{HOMO}} + E_{\text{LUMO}})}{2} \quad (3)$$

$$\eta = \frac{(\text{IE} - \text{IA})}{2} = \frac{(E_{\text{HOMO}} - E_{\text{LUMO}})}{2} \quad (4)$$

$$\omega = \frac{\mu^2}{2\eta} \quad (5)$$

$$S = \frac{1}{\eta} \quad (6)$$

The dipole moment ( $\mu$ ), mean polarizability ( $\alpha$ ) and the total first static hyperpolarizability ( $\beta_0$ ) for the compound in terms of  $x$ ,  $y$ , and  $z$  components are given by the following equations:

$$\mu = (\mu_x^2 + \mu_y^2 + \mu_z^2)^{1/2} \quad (7)$$

$$\alpha = \frac{1}{3}(\alpha_{xx} + \alpha_{yy} + \alpha_{zz}) \quad (8)$$





$$\Delta\alpha = \left[ \frac{(\alpha_{xx} - \alpha_{yy})^2 + (\alpha_{yy} - \alpha_{zz})^2 + (\alpha_{zz} - \alpha_{xx})^2}{2} \right]^{1/2} \quad (9)$$

$$\beta_0 = (\beta_{x^2} + \beta_{y^2} + \beta_{z^2})^{1/2} \quad (10)$$

and

$$\beta_0 = \beta_{xxx} + \beta_{xyy} + \beta_{xzz}$$

$$\beta_y = \beta_{yyy} + \beta_{xyx} + \beta_{yzz}$$

$$\beta_z = \beta_{zzz} + \beta_{xxz} + \beta_{yyz}$$

(or)

$$\beta_0 = [(\beta_{xxx} + \beta_{xyy} + \beta_{xzz})^2 + (\beta_{yyy} + \beta_{yzz} + \beta_{yxx})^2 + (\beta_{zzz} + \beta_{zzx} + \beta_{zyy})^2]^{1/2} \quad (11)$$

### 2.3. Characterization

FTIR was conducted on dried hydrogel samples at a scan range of 700–4000  $\text{cm}^{-1}$  at a resolution of 4  $\text{cm}^{-1}$  using a PerkinElmer (L1600300) spectrophotometer equipped with ATR under room temperature conditions with an average of 16 scans. A Seiko TG/DTA 6300 thermal analyzer was used to perform a thermogravimetric analysis (TGA) with a heating range of 30  $^{\circ}\text{C}$  to 800  $^{\circ}\text{C}$  and with a 10  $^{\circ}\text{C min}^{-1}$  heating rate. The surface morphology and pore structure of the hydrogel beads were characterized using FE-SEM, a ZEISS Sigma-300 FE-SEM unit. Swelling studies of the hydrogel beads were conducted by immersing a predetermined quantity of beads in distilled water at different pH solutions (4, 7 and 9.2) and ionic strengths (0.1 M NaCl,  $\text{CaCl}_2$  and  $\text{AlCl}_3$ ). Swelled beads were removed and weighed at regular intervals. Swelling percentage (%S) was evaluated employing eqn (12).

$$\%S = \frac{W_s - W_d}{W_d} \times 100 \quad (12)$$

where  $W_s$  and  $W_d$  represent the measured weights of swollen and dried hydrogel beads at different time intervals, respectively. All experiments were conducted in triplicate, and the average of these was reported in this paper. The mechanical strength of the hydrogel beads was determined using a TAXT Texture Analyzer (TA-HD plus, 5213, Surrey, England) equipped with a flat-bottomed plunger with a load cell of 5 kg, a cross-head shape of 1  $\text{mm s}^{-1}$  and a 0.5-inch diameter. The beads were placed on a flat-bottomed cylindrical probe of 5 kg weight to create the compression force for the test.

### 2.4. Kinetic study and adsorption isotherms

To determine the adsorption isotherms of the dye at different concentrations of the CV within the range (20–100 ppm), 0.03 L of these concentrations was added to (0.03 g) of the hydrogel in a vial at pH 9 and temperature of 25  $^{\circ}\text{C}$ . the vial was kept under continuous stirring in a water bath shaker for approximately 6 h. After a fixed time of 6 h, a small aliquot was taken out and

the dye concentration was measured on a photospectrometer ( $\lambda_{\text{max}} = 590 \text{ nm}$ ). The equilibrium adsorption capacity was calculated using a UV-vis spectrophotometer (Shimadzu 1800) using eqn (13) and (14):

$$q_e = \left( \frac{C_0 - C_t}{M} \right) \times V \quad (13)$$

$$q_t = \left( \frac{C_0 - C_t}{M} \right) \times V \quad (14)$$

where  $q_t$  and  $q_e$  ( $\text{mg g}^{-1}$ ) represent the amount of dye adsorbed by unit mass of adsorbent at a given time and after equilibrium, respectively.  $C_0$  ( $\text{mg L}^{-1}$ ) and  $C_t$  ( $\text{mg L}^{-1}$ ) represent the initial and final dye concentrations after time  $t$ , respectively.  $M$  (g) mass of the adsorbent.  $V$  represents the solution volume. Furthermore, the influence on the adsorption capacity ( $q_e$ ) using different amounts of adsorbents was evaluated by placing different amounts of prepared hydrogel beads (10–50 mg) in a model dye (30 mL) sample (30 ppm), for 6 h under constant stirring. All the said experiments were performed at pH 9, as the pH ranges of wastewater fall in this category.

**2.4.1. Kinetic modelling.** Dye adsorption by hydrogels can be described using various kinetic models. These models help understand how the dye interacts with the hydrogel over time, which is crucial for designing efficient adsorption systems. Here is a summary of the key kinetic models used:

**2.4.1.1. Pseudo-first-order kinetics.** When the adsorption process is not directly proportional to the concentration of dye (e.g., due to surface area limitations or multi-layer adsorption), a pseudo-first-order kinetic model may be applied, where the rate of adsorption depends on the surface availability of adsorption sites. The following is a synopsis of each model and its relationship to the removal of hydrogel dye:

The integrated form of the pseudo-first-order is written as eqn (15) as follows:

$$\ln(q_e - q_t) = \ln q_e - k_1 t \quad (15)$$

where  $q_t$  is the amount of dye adsorbed at time  $t$ ,  $q_e$  is the amount of dye adsorbed at equilibrium, and  $k_1$  is the pseudo-first-order rate constant. A linear plot of  $\ln(q_e - q_t)$  vs.  $t$  should yield a straight line if the process follows pseudo-first-order kinetics. This model assumes that the dye removal rate is proportional to the difference between the equilibrium amount of dye adsorbed ( $q_e$ ) and the amount adsorbed at time  $t$  ( $q_t$ ). It is useful when the adsorption rate is fast and is mainly controlled by surface interactions.

**2.4.1.2. Pseudo-second-order kinetics.** Pseudo-second-order kinetics is a widely used model for describing the rate of adsorption of substances (such as dyes) onto solid surfaces, including hydrogels. This model assumes that the adsorption rate is proportional to the square of the difference between the equilibrium concentration and the concentration at time  $t$ .



Eqn (16) is written as follows:

$$q_t = \frac{q_e^2 k_2 t}{1 + q_t k_2 t} \quad (16)$$

where  $q_t$  is the amount of dye adsorbed at time  $t$  ( $\text{mg g}^{-1}$ ),  $q_e$  is the amount of dye adsorbed at equilibrium ( $\text{mg g}^{-1}$ ), and  $k_2$  is the pseudo-second-order rate constant ( $\text{g mg}^{-1} \text{min}^{-1}$ ).

**2.4.1.3. Intra-particle diffusion kinetics.** Intra-particle diffusion kinetics is a model that describes how quickly a material (such as a dye) diffuses into the pores of a solid adsorbent, such as a hydrogel. This model is useful for understanding how the adsorption process is regulated by the diffusion of the adsorbate *via* the adsorbent's porous structure. The mathematical formula of this kinetic model is written as.

$$q_t = k_{\text{diff}} \times t^{1/2} + C \quad (17)$$

where  $q_t$  is the amount of dye adsorbed at time  $t$ ,  $k_{\text{diff}}$  is the intraparticle diffusion rate constant, and  $C$  is a constant related to the boundary layer thickness or external mass transfer resistance.

## 3. Results and discussion

### 3.1. DFT aspects

**3.1.1. Conformational study.** The optimized structure generated through DFT calculation is shown in Fig. 1. The optimized structures of GO, GG, Res and CV are shown in Fig. S1–S4 (ESI<sup>†</sup>). The target scaffold complex indicates an out-of-plane binding pattern centered at  $\text{La}^{3+}$ . The atomic assignments suggested for the complex in the optimized diagram show a bond length  $\text{La}(107)\text{--O}(119)$  of 2.35 Å. The other two  $\text{La}\text{--O}$  bonds lie in the same range, with the GO-bonded oxygen being somewhat more covalently linked. The same is explained in terms of the quantum mechanically driven binding forces involved in the sphere as given in Table 1. The results indicate that the energies involved for nuclear–nuclear interaction, electron–nuclear interaction and kinetic energy (a.u.), are respectively 2.367,  $-5.934$  and 5.344, showing the fine reactive behaviour of the complex. Similarly, the bond lengths around the coordination central atom *viz.*  $\text{O}(119)\text{--La}(107)\text{--O}(106)$ ,  $\text{O}(119)\text{--La}(107)\text{--O}(141)$ , and  $\text{O}(119)\text{--La}(107)\text{--O}(41)$  all are

Table 1 Bonding forces of atoms involved in the  $\text{La}$ -coordination sphere

Atomic assignment	Atomic number	$X$ forces (hartrees bohr <sup>-1</sup> )	$Y$ forces (hartrees bohr <sup>-1</sup> )	$Z$ forces (hartrees bohr <sup>-1</sup> )
106	8	0.164	0.027	−0.143
107	57	−0.012	0.004	−0.047
119	8	−0.044	0.005	0.016
141	8	0.047	0.013	0.016

119–120°. Therefore, the applied theory level generated satisfactory results in the context of the coordination nature of  $\text{La}^{3+}$ .

**3.1.2. FMO analysis and evaluation of global reactive descriptors.** The frontier molecular orbitals are the main reactive heads of a molecule. The respective diagram of the complex is given in Fig. 2 along with the energy gap. Fig. S1–S4 (ESI<sup>†</sup>) represent the HOMO–LUMO evaluation of the different components involved in the formation of the hydrogel and the target dye. In the case of the complex, the computed surface diagram indicates the HOMO–LUMO location towards GO of the complex. Therefore, the increased reactivity is quite evident from the orbital location and the global reactive descriptors given in Table 2. The charge separation determines the unique multipole moment as shown in the tabulated data referring to the computational analysis of hyperpolarizability. Computed multipoles may vary with the variation of the geometry of a target. The charge distribution occurring upon the exposure of a particle to an electric field is described by a set of constants called polarizabilities. These parameters have been discussed *vide infra* in relation to the adsorption of CV.

**3.1.3. CV and GO-complex adsorption mechanism through DFT.** The optimized structural parameters of the GO-complex of  $\text{La}^{3+}$  and CV show that surface modification enhances the adsorbent properties. To explain this behaviour, Mulliken

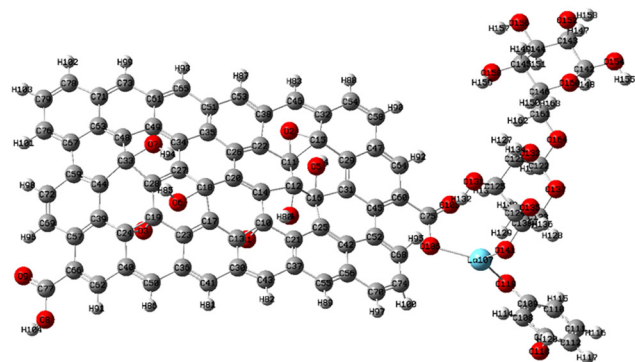


Fig. 1 Optimized structure of the GO–GG–Res– $\text{La}^{3+}$  complex.

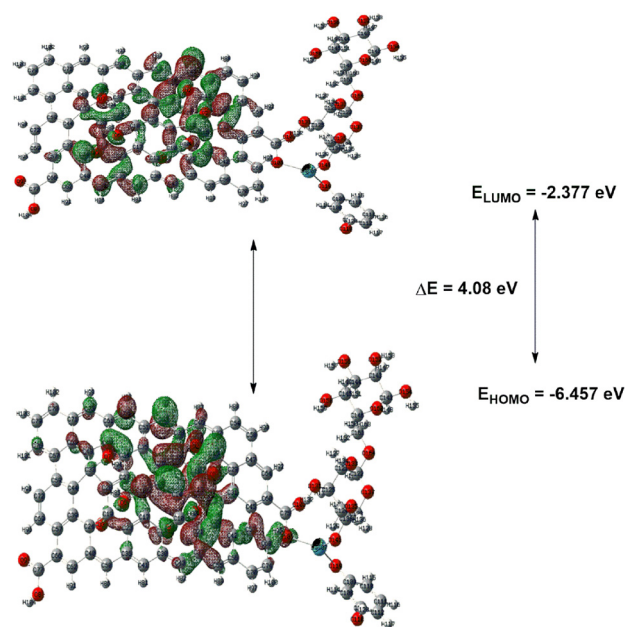


Fig. 2 HOMO–LUMO energy gap of the complex.



Table 2 Calculated global reactive descriptors and hyperpolarizability tensors

Compounds	$\eta$ (eV)	$S$ (eV)	$\omega$ (Debye eV <sup>-1</sup> )	$\mu$ (Debye)	IE (eV)	EA (eV)	$\chi_{\text{abs}}$ (eV)
GO	2.614	0.382	23.123	10.995	6.902	1.674	4.288
Res	2.952	0.339	2.051	3.480	6.068	0.164	3.116
GG	3.993	0.250	10.001	8.937	7.043	-0.944	3.049
CV	2.651	0.377	447.963	48.735	5.426	2.775	4.101
Complex	2.05	0.488	34.249	11.850	6.530	2.430	4.480
Dipole moment ( $\mu$ )				Hyperpolarizability ( $\beta$ )			
$\mu_x$		-0.495		$\beta_{xxx}$			409.985
$\mu_y$		-11.834		$\beta_{yyy}$			-536.805
$\mu_z$		-0.471		$\beta_{zzz}$			61.049
$\mu_{\text{total}}$		11.850		$\beta_{xyy}$			-499.891
Polarizability ( $\alpha$ )				$\beta_{xxy}$			-1052.356
$\alpha_{xx}$		685.775		$\beta_{xxz}$			-646.919
$\alpha_{yy}$		-653.615		$\beta_{xzz}$			185.398
$\alpha_{zz}$		-691.574		$\beta_{yzz}$			-61.172
$\alpha_{xy}$		-93.972		$\beta_{yyz}$			-102.323
$\alpha_{xz}$		-55.784		$\beta_{xyz}$			-44.367
$\alpha_{yz}$		-49.867		$\beta_0$			1758
$\alpha$ total		-219.804					
$\Delta\alpha$		1358					

charge analysis helps in discussing the regions of different non-covalent interactions in association with electrostatic interaction through electrostatic surface mapping. Mulliken charges play a significant role in understanding dye adsorption mechanisms, particularly in the context of electrostatic interactions and charge transfer. The analysis of Mulliken charges provides insights into how electron density shifts during the adsorption process, which is crucial for predicting the behavior of dye molecules on various adsorbents. In addition, the role of global reactive descriptors is helpful in this context. In Table 3 and Fig. 3, the comparison between negative and positive charges shows that the La<sup>3+</sup> on one side, and the presence of several hydrogen-bonding functionalities on ligation sites (GO, GG, and Res) are significant in CV adsorption.

The data presented in Table 3 provide valuable insights into dye adsorption. The high HOMO value and low LUMO value in

the complex compared with CV show the tendency of CV-adsorption on the hydrogel. The high HOMO–LUMO gap in the complex indicates the stability and efficiency of the adsorbent during the adsorption process. Similarly, the lower FMO gap in CV indicates a higher tendency towards electron acceptance, thereby favouring adsorption towards the complex. The dipole tensors and hyperpolarizability evaluation display that a more polar or zwitterionic nature resulting from strong ICT can lead to stronger electrostatic interactions (dipole–dipole, ion–dipole) with charged or polar adsorption sites on a substrate. This can enhance adsorption affinity and density. A similar trend is obvious from their respective global harness, global softness, and dipole tensor. These features are shown schematically in Scheme 2 to conclude the DFT-driven mechanistic approach of CV adsorption on the GO–GG–Res–La complex.

### 3.2. FTIR analysis

The FT-IR spectra obtained for samples of GG, Res, GG–Res–La, and GG–Res–La–GO hydrogel beads are shown in Fig. 4 in the range of 4000–700 cm<sup>-1</sup>. The broadband at 3272 cm<sup>-1</sup> observed in the spectrum of Res indicates the –OH stretching vibration. The peak at 1606 cm<sup>-1</sup> is attributed to the stretching vibration of aromatic C=C. The C–O stretching frequency of the Res compound occurs at 1149 cm<sup>-1</sup>, Fig. 4(a).<sup>44</sup> The FTIR study of GG is shown in Fig. 4(b). The appearance of a strong band peak at 3280.1 cm<sup>-1</sup> corresponds to hydroxyl functional group (–OH) stretching vibrations. The peak at 2926 cm<sup>-1</sup> corresponds to the –CH<sub>2</sub>– asymmetric stretching vibrations of GG, and the peaks around 1405.7 cm<sup>-1</sup> confirm the occurrence of CH stretching vibrations.<sup>45</sup> The appearance of the band at 1646 cm<sup>-1</sup> represents ring stretching vibrations, 1378 cm<sup>-1</sup> is for –CH<sub>2</sub>– deformation. The coupled stretching vibrations were approximately 750 and 1250 cm<sup>-1</sup>, indicating strongly coupled vibrations of C–O–C, C–C–O, C–OH ((1–4), (1–6)) linkage of galactose and mannose units.<sup>46–48</sup> The changes in the GG

Table 3 Atomic assignment with the Mulliken charges

Atom assignment	Mulliken charges	Atom assignment	Mulliken charges
1-O	-0.294	163-H	0.210
2-O	-0.282	106-O	-0.646
3-O	-0.275	107-La	1.245
4-O	0.092	119-O	-0.474
5-O	0.135	46-C	-0.680
6-O	-0.156	51-C	0.306
7-O	-0.310	53-C	-0.596
8-O	-0.496	131-O	-0.494
9-O	-0.319	133-O	-0.432
11-C	0.122	135-O	-0.447
15-C	-0.077	137-O	-0.260
22-C	-0.179	141-O	-0.486
26-C	-0.008	152-O	-0.491
32-C	0.496	154-O	-0.501
35-C	0.082	156-O	-0.487
38-C	0.383	158-O	-0.520
104-H	0.408	160-O	-0.280
105-O	-0.317	164-O	-0.268



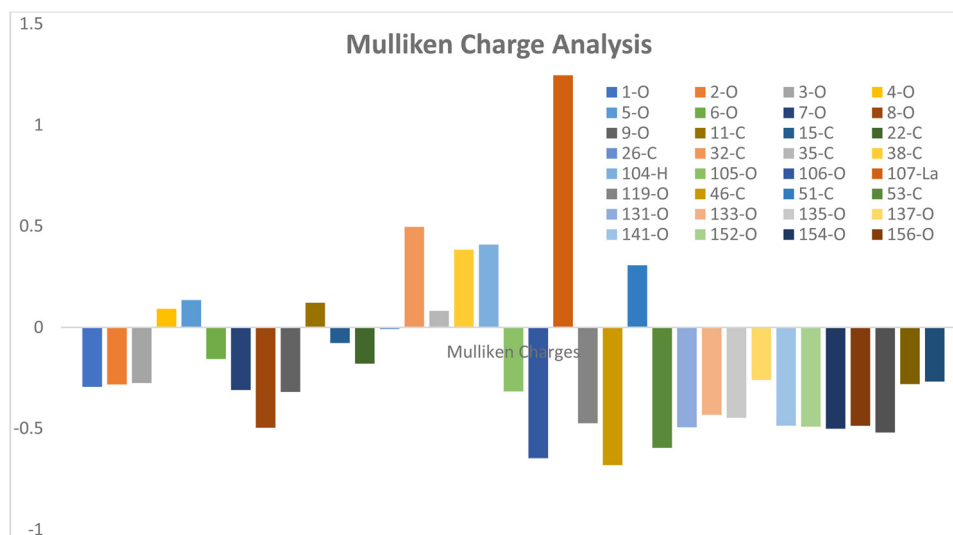
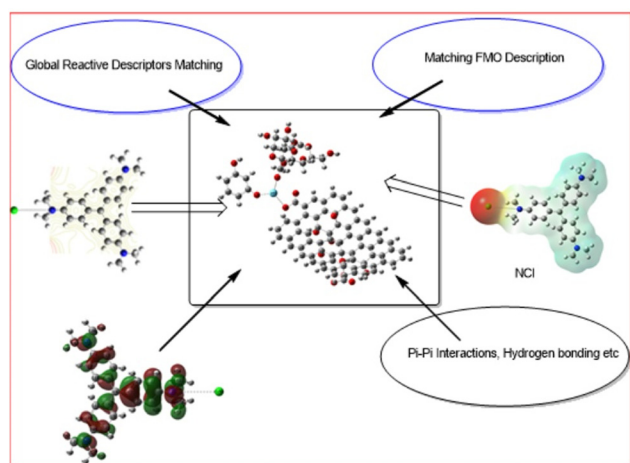


Fig. 3 Graphical representation of the Mulliken charge analysis.



Scheme 2 DFT-based mechanistic insights into the hydrogel-dye interaction.

spectrum upon the addition of  $\text{La}^{3+}(\text{aq})$  and Res are shown in Fig. 4(c). This shows that GG and Res have interacted well with the metal ion, forming a strong bead as supported by their compressive stability. The FTIR spectrum of GG-Res-La-GO shows no major shift in the peaks of GG-Res-La, suggesting the possibility of ionic interactions, as covalent bond formation is not supported by FTIR. The FTIR peak assignment table (Table 4) is given below.

### 3.3. Thermogravimetric analysis (TGA/DTA)

The thermal stability of the samples with and without GO is shown in Fig. 5. The measurements were performed at a heating rate of  $10\text{ }^{\circ}\text{C min}^{-1}$  under a nitrogen atmosphere (flow rate:  $50\text{ mL min}^{-1}$ ) using a sample mass of approximately 6.7583 mg. The hydrogel obtained by mixing GG-Res-La only shows four degradation steps with a maximum of more than

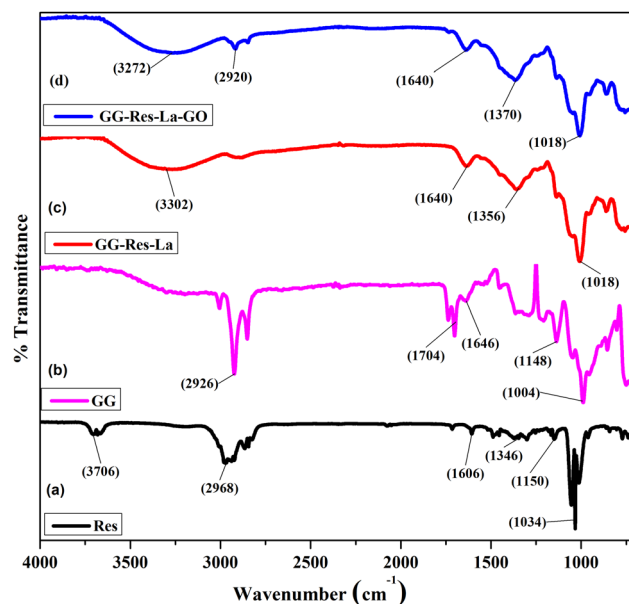


Fig. 4 FTIR spectra of the prepared hydrogel beads.

80% of degradation reported in the case of GG-Res-La without GO; however, the presence of GO increases the thermal stability of the complex, which may be possible because of the interactions between GO and the metal-containing hydrogel. All hydrogels undergo four degradation steps. The first event that is present in all of the prepared samples occurs in the range of  $80\text{--}90\text{ }^{\circ}\text{C}$ , showing above 10% weight loss that may be due to the removal of internal water present in the hydrogel. The second event is represented by the first derivative plot, as shown by the DTG plots. The second event, around  $250\text{ }^{\circ}\text{C}$ , shows a mass loss of 29%, which is related to the degradation of GG due to the weakening of glycosidic bonds in the main chain. The 3rd and 4th events are more pronounced in





Table 4 FTIR peak assignment data

Wavenumber (cm <sup>-1</sup> )	Sample(s)	Assignment
~3706	Res	O–H stretching (free hydroxyl groups)
~3302–3272	GG–Res–La/GO	O–H stretching (hydrogen-bonded –OH, GO/GG)
~2968–2926	Res, GG	C–H stretching (aliphatic chains in GG/Res)
~1704–1646	GG	C=O stretching (carbonyl groups, GG/Res crosslinking)
~1640	All composites	C=C stretching (aromatic ring in resorcinol/GO)
~1606	Res	Aromatic C=C skeletal vibration
~1370–1356	GG–Res–La, La–GO	C–O–C bending or symmetric stretching (ether linkages)
~1346	Res	C–H deformation (aromatic ring substitution)
~1150–1148	GG, Res	C–O stretching (ether or ester groups)
~1034–1018	All samples	C–O stretching (polysaccharide ring vibration in GG)
~1004	GG	Secondary alcohol C–O stretching

GG–Res–La and GG–Res–La–GO3. The 3rd and 4th events and the loss of mass may be due to the degradation of the resorcinol component and the oxidative degradation of the polymer backbone. The overall weight loss of GG–Res–La, GG–Res–La–GO1, GG–Res–La–GO2 and GG–Res–La–GO3 was approximately 83.12%, 77%, 77.4% and 79.02%, respectively. These data indicate improved packing in the presence of GO. Comparative data demonstrate that the GG–Res–La–GO2 hydrogel exhibits

an approximately 14% increase in thermal stability, as indicated by its higher final char residue (~8.1%) compared to the GG–Res–La hydrogel (~7.1%). The onset degradation temperature remained stable (~247 °C), indicating better structural retention under heat. Mechanically, GG–Res–La–GO2 showed enhanced strength, as inferred from its improved thermal profile and minimal early degradation, suggesting uniform GO dispersion and effective crosslinking. Compared with the GG–Res–La–GO1 and GO3 variants, GO2 provided a more balanced performance, avoiding early breakdown and excessive aggregation, and thus offering a ~20–30% improvement in inferred mechanical integrity over the base hydrogel. These improvements have been summarized in the revised manuscript. Thus, the use of GO to enhance the thermal stability of the prepared hydrogels is noteworthy.

### 3.4. Texture analysis

The hydrogel beads were allowed to compress to a fractional displacement under 0–100 g of load. The force–time curves for the GG–Res–La and GG–Res–La–GO samples are given in Fig. 6(a) and (b). The measured force initially increases during the loading process and decreases during the hold (relaxation) period. None of the beads were made to rupture during deformation. The behaviour of hydrogels from the plot suggests a viscoelastic character. The GG–Res–La samples showed a lower force response compared to the GG–Res–La–GO samples. The maximum compressive force sustained by the GG–Res–La–GO

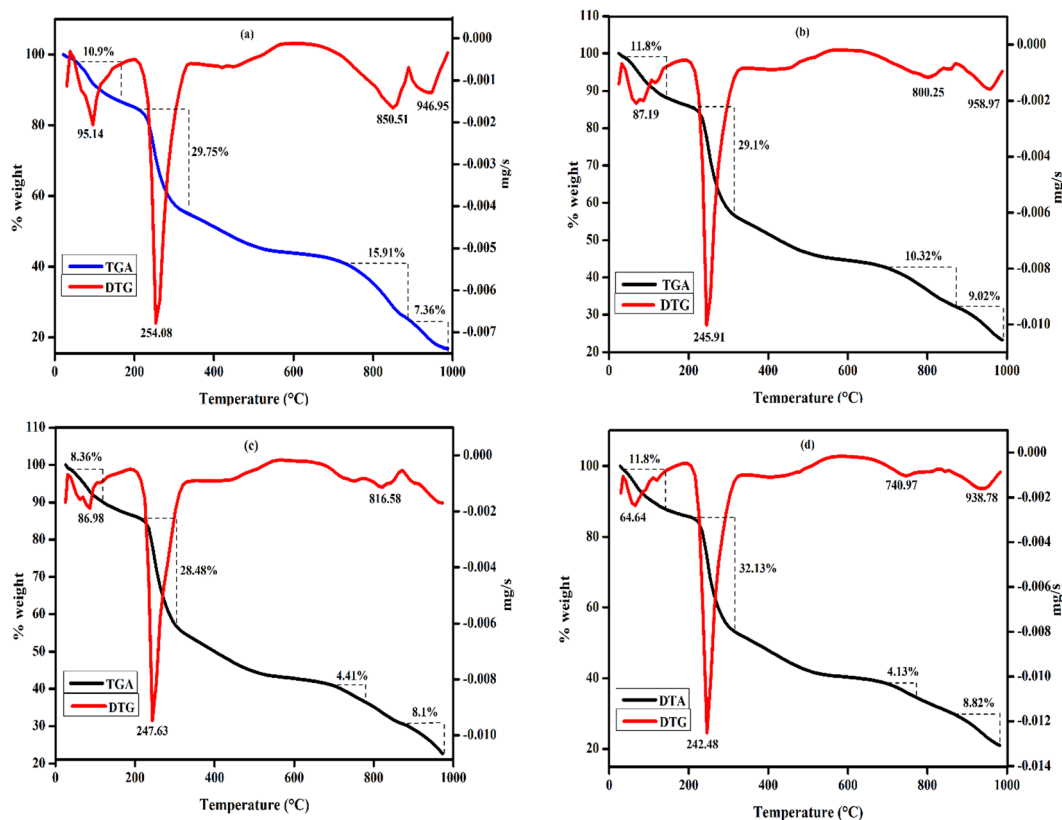


Fig. 5 TGA/DTA analysis of (a) GG–Res–La (b) GG–Res–La–GO1, (c) GG–Res–La–GO2 and (d) GG–Res–La–GO3.



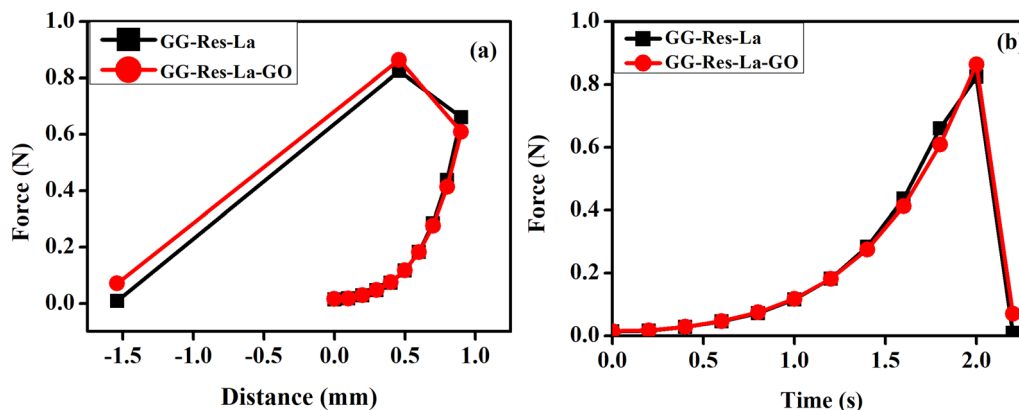


Fig. 6 Texture analysis of the prepared hydrogel beads: (a) force (N) vs. distance (mm) and (b) force (N) vs. time (mm) analyses.

hydrogel was approximately 0.88 N, compared to 0.76 N for GG-Res-La, representing a  $\sim 15.8\%$  improvement in compressive strength. This enhancement is attributed to the reinforcing effect of GO, which improves load distribution and resistance to deformation within the hydrogel matrix. Additionally, the GG-Res-La-GO hydrogel showed a more gradual and sustained increase in force over time, indicating improved elasticity and mechanical integrity. These results confirm that the incorporation of GO significantly enhances the mechanical robustness of the hydrogel, as detailed in the revised manuscript, which is consistent with previous studies.<sup>49–51</sup> The mechanical limit under compression, as observed from the force–distance curves, is indicated by the peak force before failure. Both GG-Res-La and GG-Res-La-GO samples exhibit peak forces around 0.9 N, with GG-Res-La-GO showing a slightly higher value ( $\sim 0.91$  N) compared to GG-Res-La ( $\sim 0.87$  N), suggesting improved load-bearing capacity due to the incorporation of GO. The force–distance behavior reveals an initial linear region (elastic deformation) up to  $\sim 0$  mm, followed by a nonlinear segment ( $\sim 0$ – $0.6$  mm) indicating plastic deformation. The sudden drop in force after the peak indicates a brittle-like failure or structural collapse. The same has been included in the revised manuscript.

### 3.5. SEM analysis

The surface morphology of an adsorbent plays a crucial role in determining its ability to remove dyes. To examine the surface morphology, scanning electron microscopy (SEM) was used. From the above Fig. 7(a) and (b), the hydrogel beads show a porous structure and are less rough and wrinkled, while in the case of the hydrogel beads containing GO have a rougher and more wrinkled surface. This roughness and wrinkling can be attributed to the strong crosslinking effect of the intercalated GO sheets, which formed strong hydrogen bonds with the functional groups of the polymer backbone. The presence of GO nanosheets is visible in the SEM images in Fig. 7(c) and (d).<sup>52</sup>

### 3.6. Swelling studies

One of the fundamental characteristics of hydrogels is their capacity to demonstrate a measurable volume alteration when subjected to an aqueous medium. This change can be observed

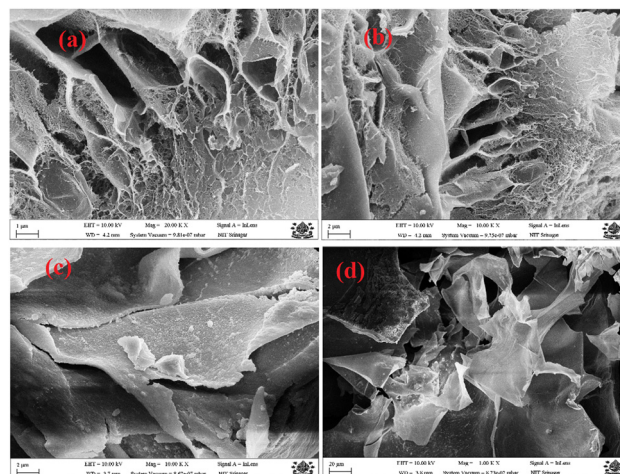


Fig. 7 SEM analysis of (a) GG-Res-La, (b) GG-Res-La-GO1, (c) GG-Res-La-GO2 and (d) GG-Res-La-GO3.

in certain hydrogels through swelling, while it is manifested in others through transitions between sol and gel phases. The hydrogel beads change from a glassy phase into a rubbery phase upon swelling. The extent of crosslinking affects the space available for diffusion within the network of the hydrogel beads, and thus it also impacts the hydrogel's ability towards swelling.<sup>53</sup> The swelling of the hydrogels was studied in different media. Approximately 30 mg of beads was immersed in 30 mL of the respective medium. The beads were removed and weighed at a regular interval of 1 hour for at least 5 h. Swelling in different media is discussed as follows:

**3.6.1. Swelling in distilled water.** Fig. 8 shows the swelling percentage of two different beads. The maximum swelling percentage was found to be 2850% and 2920% for GG-Res-La and GG-Res-La-GO hydrogel beads, respectively. The increase in swelling in GG-Res-La-GO corresponds to the addition of GO, which involves more functional groups that interact with the water molecules, mainly through physical interactions. The whole swelling experiment was conducted in triplicate, and the average swelling disposition is presented in the manuscript. The results are in accordance with our previous work.<sup>50</sup>



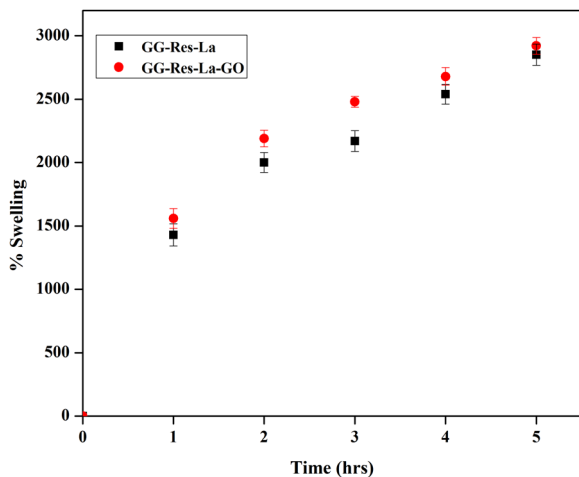


Fig. 8 Swelling percentage of GG-Res-La and GG-Res-La-GO in water.

**3.6.2. Swelling in different ionic media.** To investigate the effect of ionic strength on swelling behavior, 30 mg of the prepared hydrogel beads were immersed in 30 mL solutions of varying ionic strengths: 0.1 M NaCl, CaCl<sub>2</sub>, and AlCl<sub>3</sub>. The beads were allowed to swell for 5 h, after which the samples were removed at hourly intervals for analysis. As shown in Fig. 9, the hydrogel beads containing GO exhibited significantly higher swelling compared to those without GO. This enhanced swelling behavior is consistent with the previously discussed role of GO in improving the hydrophilicity and network structure of the hydrogel. An overall decrease in swelling was observed with increasing ionic strength. This trend is attributed to the increase in charge density in the surrounding medium, which leads to charge screening and partial neutralization of the hydrogel's fixed charges. Consequently, the electrostatic repulsion within the polymer network diminishes, resulting in pore size contraction and reduced water uptake. In the AlCl<sub>3</sub> solution, the hydrogel beads disintegrated within 1 hour of immersion. This rapid degradation is likely due to the high charge density of Al<sup>3+</sup> ions, which may disrupt the coordination interactions between the La<sup>3+</sup> ions and the

GG-Res polymer network. Interference with these metal-ligand interactions likely compromises the crosslinked structure, causing breakdown of the hydrogel matrix. The maximum swelling percentages observed were: in NaCl solution: 2070% for GG-Res-La and 2650% for GG-Res-La-GO, in CaCl<sub>2</sub> solution: 1750% for GG-Res-La and 2510% for GG-Res-La-GO, and in AlCl<sub>3</sub> solution (after 1 hour): 810% for GG-Res-La and 840% for GG-Res-La-GO, before disintegration. These results demonstrate that both ionic strength and cation valency significantly influence the swelling behavior and structural stability of the hydrogel system.

**3.6.3. Swelling in media of different pH.** The swelling behavior of the hydrogel beads was further investigated in buffer media of varying pH values—specifically pH 4 (acidic), pH 7 (neutral), and pH 9 (alkaline)—to assess the pH-responsiveness and structural stability of the hydrogels. Consistent with previous observations, hydrogel beads incorporating GO exhibited higher swelling compared to those without GO across all pH conditions. Notably, in the acidic environment (pH 4), both types of hydrogel beads began to disintegrate, with the GO-based hydrogel showing structural degradation within the first hour of immersion. The GG-Res-La beads without GO also initiated disintegration after 2 h. This behavior indicates poor structural stability of the hydrogels in strongly acidic conditions, likely due to the protonation of functional groups within the hydrogel matrix. Such protonation may disrupt the ionic and coordination crosslinking between the La<sup>3+</sup> ions and the functional groups on the GG and Res backbone, thereby weakening the network and accelerating hydrogel degradation. The influence of pH on swelling behavior is attributed to the ionization or deprotonation of hydroxyl (–OH) groups within the GG-Res matrix. At higher pH values, the removal of protons (H<sup>+</sup>) from –OH groups increases the number of negatively charged sites, potentially enhancing electrostatic repulsion within the hydrogel. However, as shown in Fig. 10, the swelling percentage decreased with increasing pH. This counter-intuitive trend may be explained by the stronger interaction of La<sup>3+</sup> ions with deprotonated –OH and other oxygen-containing moieties at higher pH levels. The enhanced ionic crosslinking results in a more rigid and compact network structure, thereby limiting water uptake and reducing the swelling ratio. These findings highlight

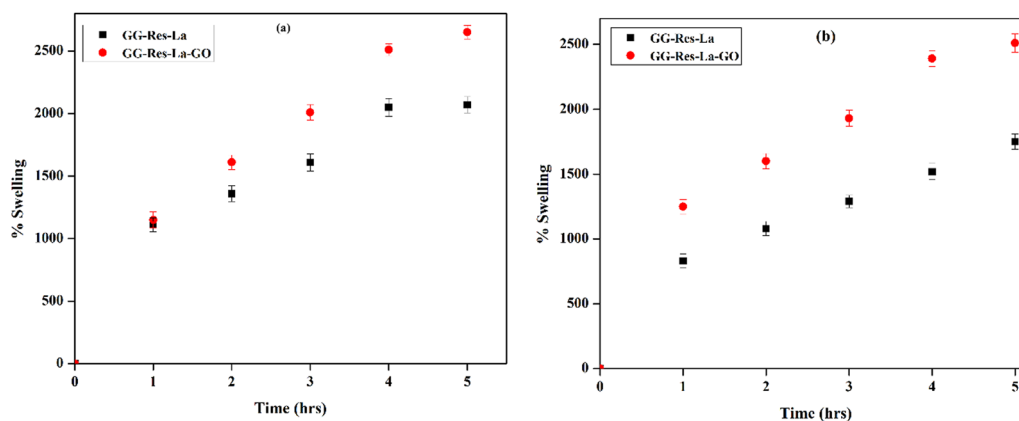


Fig. 9 Swelling in (a) NaCl and (b) CaCl<sub>2</sub> solutions.



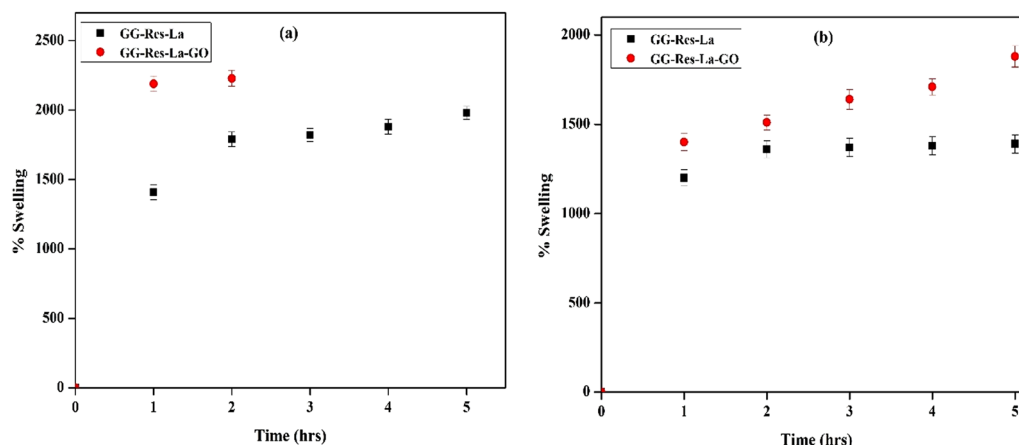


Fig. 10 Swelling at (a) pH 7 and (b) pH 9 of the media.

the dual role of pH in influencing both the chemical stability and swelling behavior of the hydrogel system, with acidic conditions promoting disintegration and alkaline conditions reinforcing crosslinking but reducing swelling capacity.

### 3.7. Adsorption of CV dye on hydrogel beads

This study aimed to examine how hydrogel beads adsorb CV dyes in an aqueous solution. Fig. 11 shows the influence of adsorption time on the dye adsorption capacity for different types of hydrogel beads. The adsorption behavior of CV in all samples can be separated into two phases. Initially, a rapid adsorption stage occurs within a short period of time, followed by a slower adsorption process. Different adsorbents have been used for the removal of CV dye from wastewater; some of them are listed in Table 1. The hydrogel beads exhibited fast adsorption rates for the first hour, after which the rates decreased gradually, eventually reaching equilibrium at around 6 h. The equilibrium adsorption amounts of the GG-Res-La, GG-Res-La-GO1, GG-Res-La-GO2 and GG-Res-La-GO3 hydrogel beads are 134.88, 234.10, 229.85 and 102.53 mg g<sup>-1</sup> of adsorbent,

respectively, indicating increased absorption ability with GO loading. The GG-Res-La-GO3 showed low adsorption due to the fact that on increasing the GO at a time, the pore structure of the hydrogel gets reduced, resulting in a decrease in the equilibrium adsorption capacity.<sup>54</sup> The high initial adsorption rates in hydrogel beads can be attributed to the presence of numerous active sites. The dyes gradually occupy these active sites, causing the adsorption rates to decrease over time. Once all the active sites are fully occupied, further adsorption does not occur even if the adsorption time is prolonged. This indicates that the adsorption equilibrium has been reached. The results demonstrate that the hydrogel beads are effective in removing CV dye within 6 h. Furthermore, the comparative analysis, as shown in Table 5, shows the promising nature of our prepared hydrogel beads.

**3.7.1. Dye removal under alkaline conditions.** The pH of the solution is one of the most important parameters affecting the adsorption process.<sup>60,61</sup> The hydrogel beads fully disintegrated at pH 4 and slightly dissociated at pH 7. Therefore, we carried out our dye removal studies at pH 9. As we already know that most of the dye-affected water has a high pH, it is necessary to study the dye adsorption at a higher pH. Fig. 12 shows the plots of CV dye adsorption at pH 9.

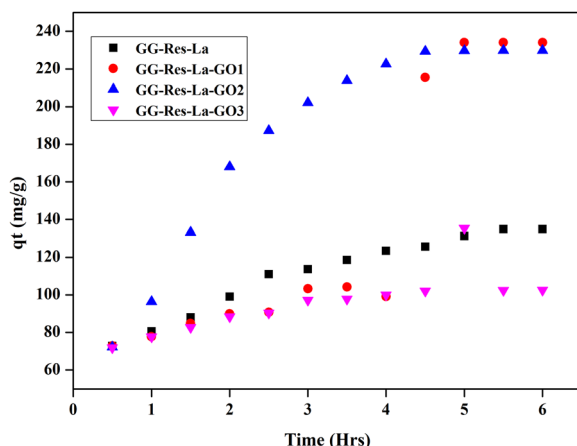


Fig. 11 Effect of adsorption time on the adsorption capacity of CV for different hydrogel beads in distilled water at room temperature.

Table 5 Comparative study of adsorption of CV dye by different adsorbents

S. no.	Adsorbent	CV dye removal (mg g <sup>-1</sup> )	Ref.
1	GG/NiWO <sub>4</sub>	170.42	55
2	Carrageenan, alginate, MMT clay	88.8	56
3	GG and polyacrylamide	6.02	57
4	Multiwalled carbon nanotubes	90.50	57
5	MoS <sub>2</sub> @bentonite	384.61	58
6	Gum arabic- <i>cl</i> -poly(acrylamide)	90.90	58
7	Poly(acrylic acid-acrylamide-methacrylate)-amylose	28.6	58
8	Poly[(2-acrylamido-2-methyl-1-propane sulfonic acid- <i>co</i> -acrylamide- <i>co</i> -acrylic acid)]	44	58
9	Polydopamine/montmorillonite/pullulan	112.45	59
10	Pearlite/ferrite/guar gum	244.40	59





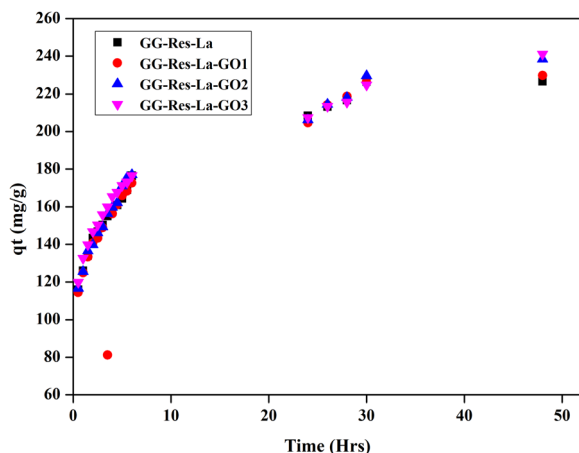


Fig. 12 Effect of adsorption time on the adsorption capacity of CV for different hydrogel beads at pH 9 and room temperature.

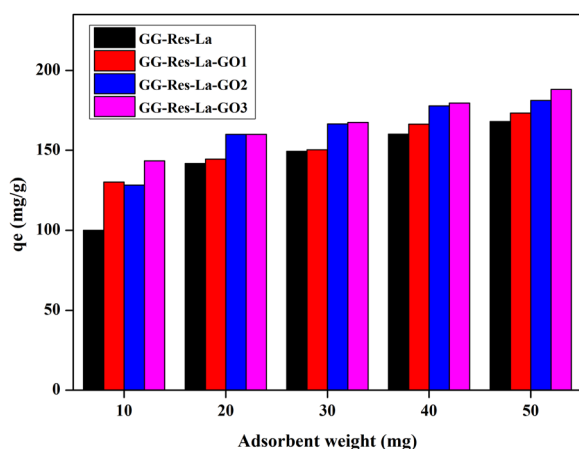


Fig. 13 Effect of adsorbent dosage on the adsorption property for CV dye.

The adsorption of CV onto the synthesized hydrogel beads is primarily governed by physical interactions. CV, a cationic dye, interacts with the negatively charged functional groups (*e.g.*,  $-\text{OH}$ ,  $-\text{COOH}$ ) present on the hydrogel surface, facilitating electrostatic attraction. Additionally, the porous structure of the hydrogel beads allows for efficient diffusion and entrapment of dye molecules, supporting a pore-filling mechanism. The  $\pi$ - $\pi$  interactions between the aromatic rings of CV and the polymeric matrix may also contribute to the overall adsorption. Based on these observations, the adsorption mechanism involves a combination of electrostatic attraction, van der Waals forces, and physical entrapment within the hydrogel matrix.

From Fig. 12, it is shown that as the time increases, the adsorption of CV also increases for the same reason. The equilibrium adsorption amounts of GG-Res-La, GG-Res-La-GO1, GG-Res-La-GO2 and GG-Res-La-GO3 hydrogel beads are  $226.66 \text{ mg g}^{-1}$ ,  $229.88 \text{ mg g}^{-1}$ ,  $238.37 \text{ mg g}^{-1}$  and  $241.09 \text{ mg g}^{-1}$  of adsorbent, respectively.

**3.7.2. Effect of the dosage change.** The effect of adsorbent dosage on the adsorption property of CV was also studied. As shown in Fig. 13, as the amount of the different hydrogel beads increases from 10–50 mg, the removal ratio of CV also increases. This suggests that with the increase of the amount of hydrogel beads in solution, the removal capacity towards dyes gradually increases. The reason for this phenomenon is attributed to the increased number of active sites for dye adsorption with the increase in the adsorbent amount, leading to increased removal.<sup>62</sup>

### 3.8. Adsorption kinetics

Adsorption kinetics is another significant measure because it reveals information about the adsorption rate and process. Dye adsorption typically involves several steps, including the penetration of dye molecules to the adsorbent surface, diffusing to internal adsorption sites, and interacting with reactive sites on the polymer backbone through chemical bonding, electrostatic interactions, ion exchange, hydrogen bonds, and hydrophobic attractions.<sup>63</sup> The hydrogels discussed herein are based on different interactions between the adsorbent and adsorbate. The hydrogel structure thus presents not only charge attractions but also  $\pi$ - $\pi$  interactions that can result in stronger binding and increased adsorption capacity. Different models, such as pseudo-first-order, pseudo-second-order and intraparticle diffusion model, were successfully applied to obtain data in water and at pH 9. Different plots obtained by applying kinetic models are briefly discussed below.

**3.8.1. Pseudo-first-order kinetics.** The calculated parameters of the pseudo-first-order kinetics are presented in Tables 6 and 7 (Fig. 14 and 15).

Table 6 Calculated parameters for pseudo 1st order kinetic models (in water)

S. no.	Hydrogel name	Slope		Intercept		$R^2$ value
		Value	Standard error	Value	Standard error	
1	GG-Res-La	−0.94418	0.14622	5.0422	0.53808	0.78722
2	GG-Res-La-GO1	−0.79825	0.17088	5.93753	0.62881	0.65434
3	GG-Res-La-GO2	−1.08701	0.07985	6.1382	0.29385	0.94368
4	GG-Res-La-GO3	−1.43037	0.16754	5.33623	0.61654	0.86729

Table 7 Calculated parameters for pseudo 1st order kinetic models (at pH 9)

S. no.	Hydrogel name	Slope		Intercept		$R^2$ value
		Value	Standard error	Value	Standard error	
1	GG-Res-La	−0.11577	0.01152	4.73968	0.20541	0.86201
2	GG-Res-La-GO1	−0.09335	0.00913	4.74343	0.12703	0.87351
3	GG-Res-La-GO2	−0.00111	$1.16551 \times 10^{-4}$	5.41095	5.41095	0.8485
4	GG-Res-La-GO3	−0.08902	0.01058	4.85476	0.18853	0.81362



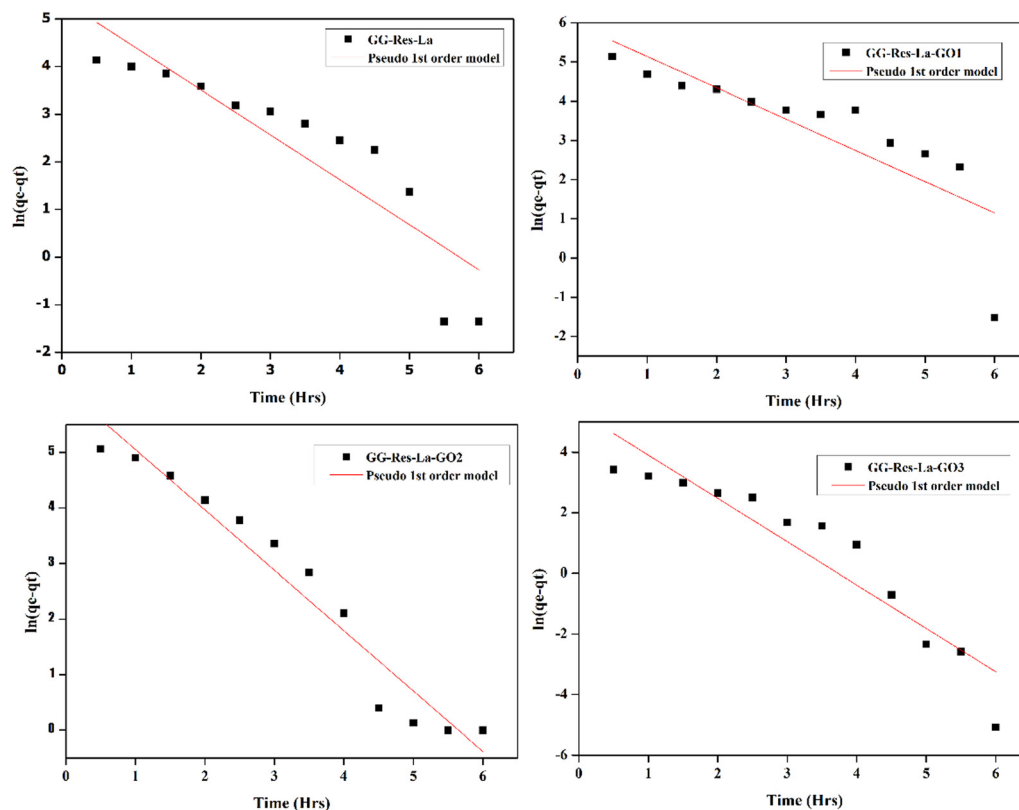


Fig. 14 Pseudo-first-order kinetic model of hydrogels in water.

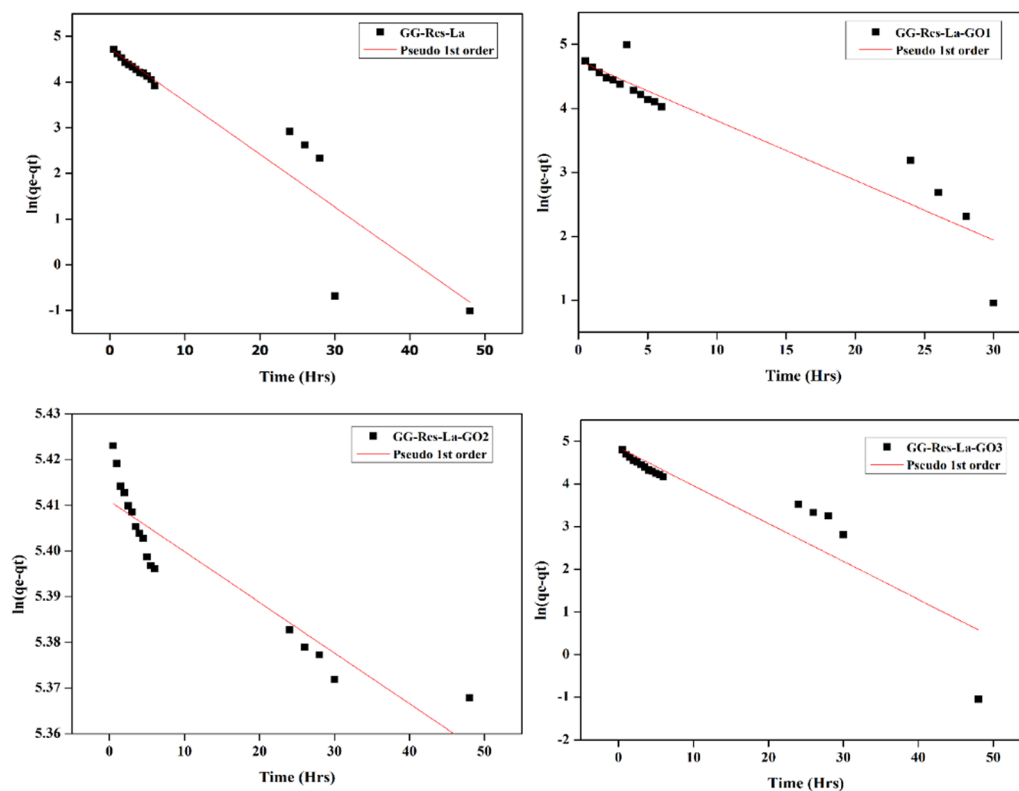


Fig. 15 Pseudo-first-order kinetic model of hydrogels at pH 9.



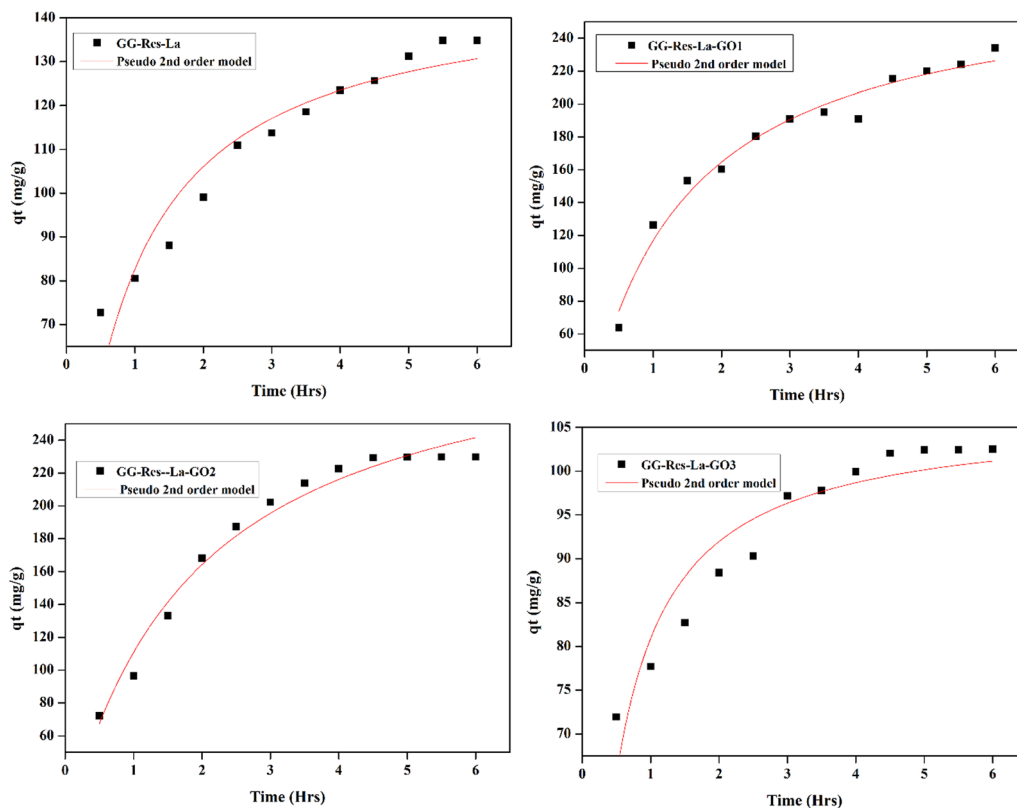


Fig. 16 Pseudo-second-order kinetics of hydrogels in water.

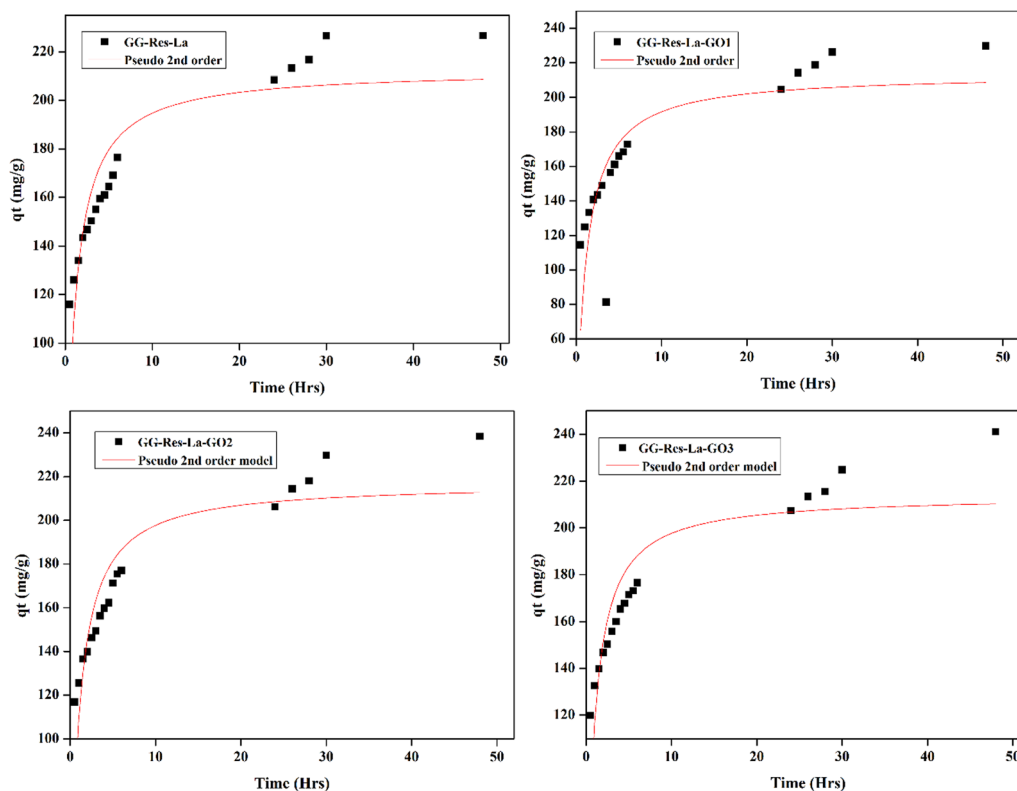


Fig. 17 Pseudo-second-order kinetics of hydrogels at pH 9.

Table 8 Calculated parameters for pseudo 2nd order models in water

S. no.	Hydrogel name	$q_e$ (mg g <sup>-1</sup> )	Standard error	$k_2$ (mol L <sup>-1</sup> )	Standard error	$R^2$ value
1	GG-Res-La	147.77211	5.64365	0.0086	0.00175	0.90236
2	GG-Res-La-GO1	278.45422	9.72314	0.0026	$3.81695 \times 10^{-4}$	0.9729
3	GG-Res-La-GO2	316.07276	12.96888	0.00171	$2.6463 \times 10^{-4}$	0.97741
4	GG-Res-La-GO3	106.47449	2.08129	0.02975	0.00488	0.88402

Table 9 Calculated parameters for Pseudo 2nd order models at pH 9

S. no.	Hydrogel name	$q_e$ (mg g <sup>-1</sup> )	Standard error	$k_2$ (mol L <sup>-1</sup> )	Standard error	$R^2$ value
1	GG-Res-La	212.67394	7.54187	0.00511	0.0011	0.78125
2	GG-Res-La-GO1	213.70725	13.02066	0.00408	0.00138	0.58199
3	GG-Res-La-GO2	217.11119	8.0238	0.00469	0.00103	0.77949
4	GG-Res-La-GO3	213.88893	7.48615	0.00569	0.00127	0.76225

**3.8.2. Pseudo-second-order kinetics.** Pseudo-second-order kinetics was performed on the obtained experimental data. The obtained plots in water and at pH 9 from the modelling are shown in Fig. 16 and 17, respectively, along with their calculated parameters in Tables 8 and 9.

**3.8.3. Intra-particle diffusion kinetics.** Intra-particle diffusion refers to the movement of adsorbates (molecules being adsorbed) within the pores or internal structure of an adsorbent material. This model helps in understanding how quickly and efficiently these molecules can diffuse through the solid material. The kinetics analysis was performed on four different samples: GG-Res-La, GG-Res-La-GO1, GG-Res-La-GO2 and GG-Res-La-GO3. These samples adsorb CV dye in water and

solutions with a pH of 9. Different plots and their calculated parameters are shown in Fig. 18, 19 and Tables 10, 11, respectively.

The kinetic and diffusion model investigation of CV dye adsorption by hydrogel beads under different circumstances (water and pH 9) demonstrates notable variations in adsorption behaviour. In the pseudo-first-order model, hydrogel efficacy is enhanced at pH 9, exhibiting elevated  $R^2$  values, notably for GG-Res-La-GO1 ( $R^2 = 0.87351$ ), signifying superior model fit. The pseudo-second-order model had a higher overall fit, particularly in water, with GG-Res-La-GO2 demonstrating the maximum adsorption capacity ( $q_e = 316.07$  mg g<sup>-1</sup>,  $R^2 = 0.97741$ ). The intra-particle diffusion model indicated a multi-step adsorption mechanism, exhibiting robust linearity for GG-Res-La ( $R^2 = 0.98226$ ) in water and GG-Res-La-GO3 ( $R^2 = 0.95839$ ) at pH 9. The integration of GO, especially in GO2 and GO3 formulations, improved the adsorption capacity and kinetics, with the pseudo-second-order model most accurately representing the process.

### 3.9. Adsorption isotherms

The GG-Res-La and GG-Res-La-GO samples exhibit various interactions that enable them to effectively adsorb dye. This is

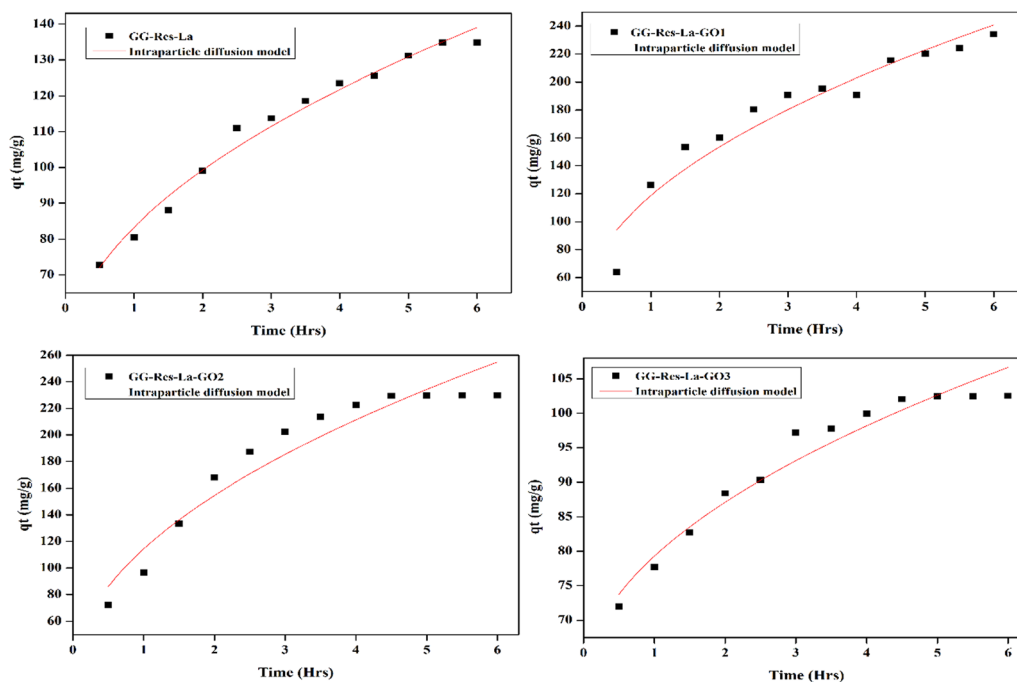


Fig. 18 Intra-particle diffusion kinetics of hydrogels in water.





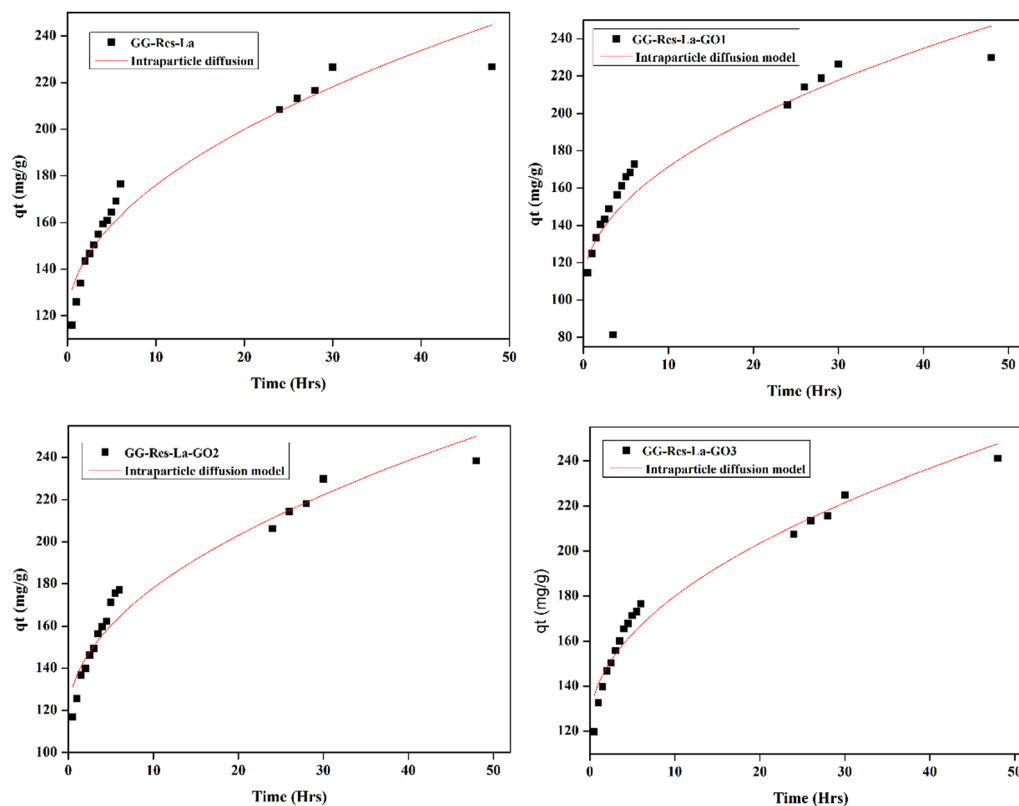


Fig. 19 Intra-particle diffusion kinetics of hydrogels at pH 9.

Table 10 Calculated parameters for intra-particle diffusion models in water

S. no.	Hydrogel name	$k_{\text{diff}}$		$C$		$R^2$ value
		Value	Standard error	Value	Standard error	
1	GG-Res-La	38.4742	1.55762	44.83078	2.80805	0.98226
2	GG-Res-La-GO1	84.30926	7.34353	34.27874	13.23874	0.92243
3	GG-Res-La-GO2	97.00076	8.67959	17.3629	15.64736	0.91846
4	GG-Res-La-GO3	18.88854	1.3015	60.39668	2.3463	0.95014

Table 11 Calculated parameters for intra-particle diffusion models at pH 9

S. no.	Hydrogel name	$k_{\text{diff}}$		$C$		$R^2$ value
		Value	Standard error	Value	Standard error	
1	GG-Res-La	18.24835	18.24835	118.29205	3.84718	0.94141
2	GG-Res-La-GO1	20.0577	2.516	107.95702	8.52126	0.796320
3	GG-Res-La-GO2	19.11732	1.12233	117.5658	3.80113	0.94757
4	GG-Res-La-GO3	17.96786	0.93469	123.11215	3.16562	0.95839

attributed to their unique microstructures and high concentration of hydroxyl groups. The CV adsorption isotherms for the adsorption process of hydrogel beads are presented in Fig. 20. As the concentration of the CV dye increases, the absorption rate on the hydrogel beads also increases rapidly.

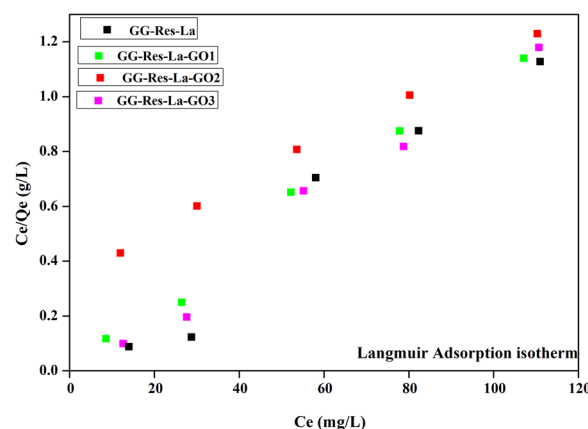


Fig. 20 Langmuir adsorption isotherm for GG-Res-La and GG-Res-La-GO hydrogels.

However, as the concentration increases, the rate of absorption decreases due to the saturation of active sites on the absorbent. The GG-Res-La-GO hydrogel beads show higher  $q_e$  values for CV solutions than GG-Res-La, indicating that the incorporation of GO results in increased absorption ability. Furthermore, Table 12 provides the details of parameters related to Langmuir isotherms applied for dye removal studies using GG-Res-La and GG-Res-La-GO based hydrogels.

Table 12 Different calculated parameters of the applied Langmuir isotherm

S. no.	Hydrogel name	Intercept		Slope		$R^2$	$Q_{\max}$ (mg g <sup>-1</sup> )
		Value	Standard error	Value	Standard error		
1	GG-Res-La	0.3518	0.0421	0.0081	$8.73 \times 10^{-5}$	0.9972	123.45
2	GG-Res-La-GO1	0.319	0.0218	0.0071	$7.7817 \times 10^{-4}$	0.9848	142.85
3	GG-Res-La-GO2	0.3346	0.0891	0.0044	0.00186	0.987	227.27
4	GG-Res-La-GO3	0.3141	0.042	0.0056	$8.738 \times 10^{-4}$	0.967	178.57

## 4. Conclusion

Hydrogels of polymers containing GO nanosheets are sought-after materials for environmental applications because of their high adsorption capacity. We reported a composite hydrogel containing double-cross-linked polymer networks containing GG and Res. The hydrogel showed good removal capacity for CV dye and may be used for the removal of other harmful dyes from waste and aqueous waters. Through DFT calculations, the optimized framework and several reactive descriptors reveal the key characteristics of the complex. The presence of hydrophilic guar gum and Res ensures strong interaction with dye molecules *via* hydrogen bonding. The maximum removal capacity for GG-Res-La and GG-Res-La-GO2 hydrogels at room temperature was 123.0 and 227.26 mg g<sup>-1</sup>, respectively, using the Langmuir isotherm. The comparative data show that the GO-based hydrogel achieved an 84.79% higher adsorption capacity than the GG-Res-La (without GO) hydrogel. This paper can serve as a good base for different environmental applications, particularly in removing dyes from aqueous media. This article shows that the adsorbent is a potential agent for dye remediation.

## Conflicts of interest

There are no conflicts to declare.

## Data availability

The authors confirm that the data supporting the findings of this study are available within the article.

## References

- Z. Zhang, P. Tran, S. Rumi, N. Bergfeld, T. W. Reid and N. Abidi, *Int. J. Biol. Macromol.*, 2024, **280**, 135908.
- K. N. Maroulas, P. Efthymiopoulos, V. Iliadou, A. Zamboulis, N. D. Bikiaris, E. Bakalis and G. Z. Kyzas, *J. Ind. Eng. Chem.*, 2025, **142**, 309–320.
- Y. Zhang, K. Kobayashi, R. Kusumi, U.-J. Kim and M. Wada, *Colloids Surf., A*, 2024, **682**, 132859.
- Z. Aksu, *Process Biochem.*, 2005, **40**, 997–1026.
- Y. Badr, M. G. Abd El-Wahed and M. A. Mahmoud, *J. Hazard. Mater.*, 2008, **154**, 245–253.
- M. K. N. Mohd Zuhan, S. Azhari and M. A. Tamar Jaya, *Sci. Res. J.*, 2021, **18**, 177–213.
- C. Liu, H. Liu, T. Xiong, A. Xu, B. Pan and K. Tang, *Polymers*, 2018, **10**, 835.
- Ş. Parlayıcı, *J. Anal. Sci. Technol.*, 2019, **10**, 1–15.
- M. Caldera-Villalobos, D. A. Cabrera-Munguía, T. E. Flores-Guía, G. Viramontes-Gamboa, J. A. Vargas-Correa, L. F. Cano-Salazar and J. A. Claudio-Rizo, *J. Polym. Res.*, 2021, **28**, 1–19.
- B. Swanckaert, J. Geltmeyer, K. Rabaey, K. De Buysser, L. Bonin and K. De Clerck, *Sep. Purif. Technol.*, 2022, **287**, 120529.
- M. Caldera-Villalobos, J. A. Claudio-Rizo, D. A. Cabrera-Munguía and N. G. Burciaga-Montemayor, *Water Environ. Res.*, 2022, **94**, e10785.
- N. Peng, D. Hu, J. Zeng, Y. Li, L. Liang and C. Chang, *ACS Sustainable Chem. Eng.*, 2016, **4**, 7217–7224.
- O. Duman, T. G. Polat, C. Ö. Diker and S. Tunç, *Int. J. Biol. Macromol.*, 2020, **160**, 823–835.
- F. Z. Choumane, B. Benguela, B. Maachou and N. Saadi, *Ecol. Eng.*, 2017, **107**, 152–159.
- X. Wang, Z. Wang, H. Chen and Z. Wu, *J. Hazard. Mater.*, 2017, **339**, 182–190.
- A. Kumar, G. Sharma, M. Naushad, T. Ahamad, R. C. Veses and F. J. Stadler, *Chem. Eng. J.*, 2019, **370**, 148–165.
- G. Sharma, A. Kumar, M. Naushad, B. Thakur, D.-V. N. Vo, B. Gao, A. A. Al-Kahtani and F. J. Stadler, *J. Hazard. Mater.*, 2021, **416**, 125714.
- M. Ahmaruzzaman, P. Roy, A. Bonilla-Petriciolet, M. Badawi, S. V. Ganachari, N. P. Shetti and T. M. Aminabhavi, *Chemosphere*, 2023, **331**, 138743.
- A. A. Kouzoutoglou-Efremidou, A. K. Tolkou, K. N. Maroulas, R. I. Kosheleva, I. A. Katsoyiannis and G. Z. Kyzas, *Langmuir*, 2025, **41**(5), 3603–3622.
- R. Sharma, B. S. Kaith, S. Kalia, D. Pathania, A. Kumar, N. Sharma, R. M. Street and C. Schauer, *J. Environ. Manage.*, 2015, **162**, 37–45.
- A. Abdelaziz, S. El-Saeed, E. Zaki, M. Abdel-Raouf and A. Al-Sabagh, *Egypt. J. Chem.*, 2021, **64**, 7551–7564.
- M. Usman, M. B. Taj and S. A. C. Carabineiro, *Environ. Sci. Pollut. Res.*, 2023, **30**, 102027–102046.
- V. Vaid, Khushbu, Nikhil, N. Dagar and R. Jindal, *ChemistrySelect*, 2022, **7**, e202203138.
- F. Simran, P. Karumbaiah, P. Roy and R. R. N. Sailaja, *Adv. Mater. Lett.*, 2022, **13**, 1686–2201.
- S. Yadav, A. Asthana, A. K. Singh, R. Chakraborty, S. Sree Vidya, A. Singh and S. A. C. Carabineiro, *Nanomaterials*, 2021, **11**, 568.



- 26 H. Zhang, X. Pang and Y. Qi, *RSC Adv.*, 2015, **5**, 89083–89091.
- 27 O. Mouhtady, E. Obeid, M. Abu-Samha, K. Younes and N. Murshid, *Gels*, 2022, **8**, 447.
- 28 Y. Liu, S. Huang, X. Zhao and Y. Zhang, *Colloids Surf., A*, 2018, **539**, 1–10.
- 29 B. Li and H. Yin, *J. Dispersion Sci. Technol.*, 2021, **42**, 1830–1842.
- 30 E. Kusurini, B. Wicaksono, Y. Yulizar, E. A. Prasetyanto and C. Gunawan, *IOP Conference Series: Materials Science and Engineering*, IOP Publishing, 2018, vol. 316, p. 12029.
- 31 P. Carloni, F. U. Alber and F. Alber, *Quantum Medicinal Chemistry*, John Wiley & Sons, 2003, vol. 17.
- 32 D. C. Carrascal-Hernandez, M. Mendez-Lopez, D. Insuasty, S. García-Freites, M. Sanjuan and E. Márquez, *Gels*, 2024, **10**, 386.
- 33 A. Allangawi, M. A. A. Aljar, K. Ayub, A. Abd El-Fattah and T. Mahmood, *J. Mol. Graphics Modell.*, 2023, **122**, 108468.
- 34 S. Pashaei-Fakhri, S. J. Peighambaroust, R. Foroutan, N. Arsalani and B. Ramavandi, *Chemosphere*, 2021, **270**, 129419.
- 35 R. Ahmad and M. O. Ejaz, *Dyes Pigm.*, 2023, **216**, 111305.
- 36 P. L. Homagai, R. Poudel, S. Poudel and A. Bhattarai, *Heliyon*, 2022, **8**(4), e09261.
- 37 D. C. Marcano, D. V. Kosynkin, J. M. Berlin, A. Sinitskii, Z. Sun, A. Slesarev, L. B. Alemany, W. Lu and J. M. Tour, *ACS Nano*, 2010, **4**, 4806–4814.
- 38 J. R. Beryl and J. R. Xavier, *J. Mater. Sci.*, 2024, **59**, 458–490.
- 39 N. Jeeva, K. Thirunavukkarasu and J. R. Xavier, *Diamond Relat. Mater.*, 2024, **142**, 110792.
- 40 J. R. Xavier, S. P. Vinodhini and J. R. Beryl, *Mater. Today Commun.*, 2024, **38**, 107842.
- 41 R. Tyagi, V. Kumar, P. Sharma and R. Nautiyal, *Chemistry-Select*, 2021, **6**, 8709–8715.
- 42 I. D. Alonso-Buenaposada, L. Garrido, M. A. Montes-Morán, J. A. Menéndez and A. Arenillas, *J. Sol-Gel Sci. Technol.*, 2017, **83**, 478–488.
- 43 C. J. Brabec and N. S. Sarici, *Adv. Funct. Mater.*, 2001, **11**, 15–26.
- 44 R. Govindasamy and S. Ayappan, *J. Chil. Chem. Soc.*, 2015, **60**, 2786–2798.
- 45 A. Chetouani, N. Follain, S. Marais, C. Rihouey, M. Elkolli, M. Bounekhel, D. Benachour and D. Le Cerf, *Int. J. Biol. Macromol.*, 2017, **97**, 348–356.
- 46 G. Sen, S. Mishra, U. Jha and S. Pal, *Int. J. Biol. Macromol.*, 2010, **47**, 164–170.
- 47 D. Mudgil, S. Barak and B. S. Khatkar, *Int. J. Biol. Macromol.*, 2012, **50**, 1035–1039.
- 48 D. Lakshmi, S. Rajendran, J. Sathiyabama, R. J. Rathis and S. S. Prabha, *Int. J. Nano Corros. Sci. Eng.*, 2016, **3**, 181–203.
- 49 S. Stößlein, I. Grunwald, J. Stelten and A. Hartwig, *Carbohydr. Polym.*, 2019, **205**, 287–294.
- 50 R. A. Rather, M. A. Bhat and A. H. Shalla, *Chem. Eng. Res. Des.*, 2022, **182**, 604–615.
- 51 M. Ø. Olderøy, M. Xie, J.-P. Andreassen, B. L. Strand, Z. Zhang and P. Sikorski, *J. Mater. Sci.: Mater. Med.*, 2012, **23**, 1619–1627.
- 52 M. Rasoulzadeh and H. Namazi, *Carbohydr. Polym.*, 2017, **168**, 320–326.
- 53 R. Subramani, A. Izquierdo-Alvarez, P. Bhattacharya, M. Meerts, P. Moldenaers, H. Ramon and H. Van Oosterwyck, *Front. Mater.*, 2020, **7**, 212.
- 54 Q. Peng, M. Liu, J. Zheng and C. Zhou, *Microporous Mesoporous Mater.*, 2015, **201**, 190–201.
- 55 D. Hussain, S. A. Khan and T. A. Khan, *Colloid Interface Sci. Commun.*, 2021, **44**, 100488.
- 56 G. R. Mahdavinia, H. Aghaie, H. Sheykhoie, M. T. Vardini and H. Etemadi, *Carbohydr. Polym.*, 2013, **98**, 358–365.
- 57 J. N. Hiremath and B. Vishalakshi, *Polym. Bull.*, 2015, **72**, 3063–3081.
- 58 M. K. Uddin, F. Mashkoor, I. M. AlArifi and A. Nasar, *Mater. Res. Bull.*, 2021, **139**, 111279.
- 59 X. Qi, Q. Zeng, X. Tong, T. Su, L. Xie, K. Yuan, J. Xu and J. Shen, *J. Hazard. Mater.*, 2021, **402**, 123359.
- 60 H.-Y. Zhu, Y.-Q. Fu, R. Jiang, J. Yao, L. Xiao and G.-M. Zeng, *Bioresour. Technol.*, 2012, **105**, 24–30.
- 61 H. Y. Zhu, R. Jiang, L. Xiao and G. M. Zeng, *Bioresour. Technol.*, 2010, **101**, 5063–5069.
- 62 H. Liu, B. Pan, Q. Wang, Y. Niu, Y. Tai, X. Du and K. Zhang, *Chemosphere*, 2021, **263**, 128240.
- 63 B. Salunkhe and T. P. Schuman, *Macromol.*, 2021, **1**, 256–275.

